LAPPEENRANTA UNIVERSITY OF TECHNOLOGY

LUT School of Energy Systems

LUT Mechanical Engineering

*Neda Neisi*

**STRESSES IN A TOUCHDOWN BEARING DURING DROPDOWN EVENT**

Examiners: Professor Jussi Sopanen

                D. Sc. (Tech.) Emil Kurvinen

**ABSTRACT**

Lappeenranta University of Technology
LUT School of Energy Systems
LUT Mechanical Engineering

Neda Neisi

**Stresses in a Touchdown Bearing During Dropdown Event**

Master's thesis

2016

62 Pages, 35 Figures and 7 Tables

Examiners: Professor Jussi Sopanen

D. Sc. (Tech.) Emil Kurvinen

Keywords: Touchdown bearing, Dropdown, Hertzian Stress, Normal force, Deformation.

Active magnetic bearing has many advantages over the conventional bearing and many industries have become interested to utilize the active magnetic bearing in their system. However, this system is very sensitive to absence of magnetic field. The touchdown bearing is protecting the rotor from the failure in the dropdown. During the dropdown the rotor contacts the touchdown bearing and the bearing experiences high level of stress. In order to estimate the life time of the touchdown bearing, the stress that is imposed to the touchdown bearing should be taken into account. The Hertzian stress is an analytical method that can be applied to obtain the stress in an infinitesimal contact area between the ball and bearing race. In this method instead of the point contact between ball and race, an elliptic area as a result of projection of the contact bodies will be used to calculate the stress. The normal force between the ball and bearing race depends on the contact stiffness and deformation of the bearing race in dropdown. The deformation can be obtained with the help of the simulation of the dropdown and the models for the ball bearing. Current study applies Hertzian contact stress theory to investigate the stress level for the rotor bearing system that is selected for case study.

## ACKNOWLEDGEMENTS

First of all, I wish to thank Professor Aki Mikkola and Professor Jussi Sopanen for their invaluable kindness and their excellent guidance during my study.

I would like to thank D. Sc. (Tech.) Emil Kurvinen, for his enthusiasm, guidance, patience and technical advices during the thesis. I am also grateful for D. Sc. (Tech.) Janne Heikkinen for his encouragement and valuable comments in the early stage of this research.

I express my gratitude to my parents and my brothers for their unconditional love, inspiration, encouragement and extensive support during my study.

Neda Neisi

Lappeenranta 25.01.2016

## TABLE OF CONTENTS

# LIST OF SYMBOLS AND ABBREVIATIONS

| | |
|---|---|
| $A$ | Inverse of the effective radius of curvature in $x$-direction |
| $A^*$ | Cross section of the beam element |
| $a$ | Semi-major axis of the elliptic area |
| $a_{0\dots3}$ | Coefficient of polynomial shape function |
| $a^*$ | Dimensionless form of $a$ |
| $B$ | Inverse of the effective radius of curvature in $y$-direction |
| $b$ | Semi-minor axis of the elliptic area |
| $b_{0\dots3}$ | Coefficient of polynomial shape function |
| $b^*$ | Dimensionless form of $b$ |
| $\mathbf{C}$ | Damping matrix |
| $c$ | Arbitrary fixed length |
| $C_b$ | Bearing damping coefficient |
| $c_d$ | Bearing diametric clearance |
| $D$ | Diameter |
| $D_h$ | Bearing outer diameter |
| $d$ | Diameter of the ball |
| $d_s$ | Bore diameter |
| $d_m$ | Bearing pitch diameter |
| $\acute{d}$ | Distance between inner race and outer race |
| $E$ | Modulus of elasticity |
| $E^*$ | Effective Modulus of elasticity |
| $e$ | Eccentricity |
| $\mathbf{F}$ | Vector of externally applied force |
| $\mathbf{F}_{tot}$ | Sum of the vectors of externally applied force |
| $F(\rho)$ | Auxiliary function |
| $f$ | Conformity ratio |
| $\mathbf{G}$ | Gyroscopic matrix |
| $G$ | Shear modulus of elasticity |
| $\mathbf{g}$ | Intermediate gyroscopic matrix |

| | |
|---|---|
| $h_o$ | Oil film thickness |
| $I$ | Moment of inertia |
| $\mathbf{K}$ | Stiffness matrix |
| $K_c$ | Contact stiffness |
| $K_s$ | Shear correction factor |
| $L$ | The difference between the kinetic and potential energy |
| $L_e$ | Length of element |
| $l$ | Arbitrary fixed length |
| $\mathbf{M}$ | Mass matrix |
| $M$ | Momentum |
| $N$ | Number of balls carrying the load |
| $\mathbf{N}(s)$ | Shape function matrix |
| $n$ | Number of balls |
| $\mathbf{P}$ | Vector of modal coordinate |
| $\mathbf{Q}_e$ | Vector of externally applied forces |
| $\mathbf{Q}_1$ and $\mathbf{Q}_2$ | Force vector describing the mass unbalance rotor |
| $Q$ | Normal force |
| $\mathbf{q}$ | Vector of generalized coordinate |
| $R$ | Radius |
| $r$ | Radius |
| $S$ | Principal stress |
| $S_o$ | The largest positive root of the equation 2.44 |
| $s$ | Longitudinal coordinate |
| $T$ | Kinetic energy |
| $U$ | Strain energy of element |
| $U^*$ | Arbitrary function |
| $u$ | Local coordinate |
| $u^*$ | Deformation in $x$-direction |
| $V$ | Shear force |
| $V^*$ | Arbitrary function |
| $v$ | Local coordinate |
| $v^*$ | Deformation in $y$-direction |

| | |
|---|---|
| W | Bearing width |
| $w^*$ | Deformation in $z$-direction |
| $X$ | Dimensionless parameter in $x$-direction |
| $x$ | Principal distance in $x$-direction |
| $Y$ | Dimensionless parameter in $y$-direction |
| $y$ | Principal distance in $y$-direction |
| $Z$ | Dimensionless parameter in $z$-direction |
| $z$ | Principal distance in $z$-direction |
| | |
| $\beta_j$ | Azimuth angle |
| $\Gamma$ | Misalignment |
| $\gamma$ | Shear strain/rotation strain |
| $\delta$ | Deformation of contact area |
| $\delta^*$ | Dimensionless form of $\delta$ |
| $\varepsilon$ | Normal strain |
| $\bar{\zeta}$ | Elliptic integral of the second kind |
| $\theta$ | Rotational degree of freedom / angle |
| $\vartheta$ | Auxiliary angle |
| $\kappa$ | Elliptic eccentricity parameter |
| $\nu$ | Poisson's ratio |
| $\bar{\xi}$ | Elliptic integral of the first kind |
| $\rho$ | Density |
| $\sigma$ | Stress |
| $\sigma_{max}$ | Maximum contact stress |
| $\sigma_o$ | Stress at center of geometry |
| $\sigma_r$ | Radial stress |
| $\tau$ | Shear stress |
| $\boldsymbol{\Phi}$ | Modal matrix |
| $\varphi$ | Contact angle |
| $\Omega$ | Angular velocity of the rotor |

**Subscript**

| | |
|---|---|
| $b$ | Ball or bending |
| $d$ | Diametrical |
| $e$ | Effective |
| $I$ | Contact body I |
| $II$ | Contact body II |
| $Ix$ | Contact body I in $x$-direction |
| $IIx$ | Contact body II in $x$-direction |
| $Iy$ | Contact body I in $y$-direction |
| $IIy$ | Contact body II in $y$-direction |
| $i/in$ | Inner race |
| $j$ | $j^{\text{th}}$ ball |
| $o/out$ | Outer race |
| $p$ | Polar |
| $R$ | Rotational coordinate |
| $r$ | Radial |
| $s$ | Shear |
| $T$ | Translational coordinate |
| $u$ | Local coordinate of element in $x$-direction |
| $v$ | Local coordinate of element in $y$-direction |
| $x$ | $x$-direction |
| $xy$ | $xy$-plane |
| $xz$ | $xz$-plane |
| $y$ | $y$-direction |
| $yz$ | $yz$-plane |
| $z$ | $z$-direction |

**Superscripts**

| | |
|---|---|
| $e$ | Element |
| $in$ | Inner race |
| $out$ | Outer race |
| $r$ | Radial |

| | |
|---|---|
| *t* | Axial |
| tot | Total |

| | |
|---|---|
| AMB | Active Magnetic Bearing |
| FEM | Finite Element Method |
| HRC | Rockwell C-Scale Hardness |
| LUT | Lappeenranta University of Technology |
| RoBedyn | Rotor-Bearing Dynamics tool box for Matlab |

# 1  INTRODUCTION

This chapter introduces the main reasons of applying touchdown bearing, previous studies on the developing various models for the dropdown and touchdown bearing. Then, the brief description about the obstacles on estimating the stress of the touchdown bearing and the methods to overcome the problem will be provided.

## 1.1 Background

In AMB (Active Magnetic Bearing), the rotor is suspended in the magnetic field and the friction between the rotor and the bearing does not exist. In this system, the position of the rotor can be controlled by feedback control of AMB. Therefore, the dynamic properties (stiffness and damping) of the system can be regulated. Controlling the natural frequencies and vibration of the rotor are supplementary advantages of applying the AMB. Moreover, the active feedback control of the system enables the unbalance compensation of the rotor during the operating condition. [1, p.601.] Although the AMB has many advantages in comparison to the conventional bearing, it is extremely sensitive to the absence of magnetic field. Therefore, providing an appropriate protection device which keeps the rotor intact from the failure of AMB is an essential requirement of the system. Touchdown bearings are the only devices preventing rotor from the probable failure in the dropdown event. Touchdown bearing might also be in service while the AMB is in operation or it is overloaded. [2, p. 692.] The touchdown bearing used for protection of the rotor during the dropdown also named as auxiliary bearing, retainer bearing, catcher bearing or backup bearing. In industrial applications, ball bearing is dominated for touchdown bearing mainly for minimizing energy dissipation, the rapid acceleration of inner race and decreasing the whirling motion of the rotor [1, p. 602; 3, pp.406-413]. Figure 1.1 shows the schematic of the touchdown bearing and AMB of the turbo expander for energy recovery from natural gas [4, p.20].
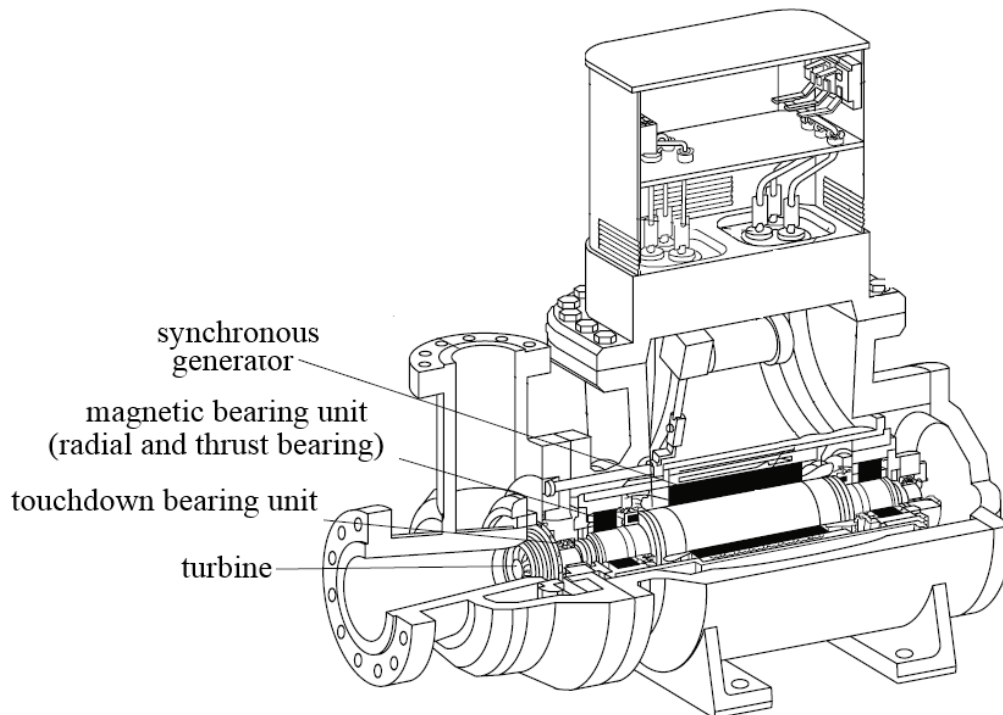
**Figure 1.1.** Schematic of the touchdown bearing and magnet bearing [Mod. 4, p.20].

Recent developments in the field of AMB have led to an interest in simulation of rotor during dropdown and selecting an appropriate design model for touchdown bearing. These studies indicate that FEM (Finite Element Method) is an accurate model for rotor. But, applying the FEM for modeling nonlinearity in the bearing is computationally time consuming. The models for rotor dropdown in touchdown bearing combining the FEM and modal reduction are efficient in reducing the computational time. In addition, the literature provides information about the detail of bearing model, stiffness and damping of the support, oil film, friction coefficient and inertia of rolling element. [1, pp. 601-617; 2, pp. 692-705.]

In the literature, several models for ball bearings have been proposed to explain the gyroscopic effect and the centrifugal forces. Kurvinen et al. [5, pp. 240-260] improved the model provided by Sopanen and Mikkola [6, pp. 201-211; 7, pp. 213-223] and added the centrifugal forces and gyroscopic moment and contemplated the defect in the ball bearings. Kärkkäinen et al. [1, pp. 606-608] considered rotational inertia of the ball and inner ring and aerodynamic torque. In a recent paper of Halminen et al. [2, pp. 692-705] the model for the

cageless bearing is developed based on the available model for the bearing with the cage. The friction between the rotor and inner race will affect the whirling motion of the rotor [1, p. 613; 8, pp. 79-89]. As a result of the wear between the rotor and inner race in dropdowns and also the thermal growth of bearing, the friction coefficient might change during the life time of touchdown bearing [9, pp. 334-359; 10, pp. 505-517]. In addition to the friction coefficient, the stiffness and damping, mass of the support and the rotor imbalance influences the behavior of the rotor in dropdown. Moreover, the optimal design of the damping, effect of damping in dynamic response of system, air gap clearance, friction coefficient and comparison of double row ball bearing and single row ball bearing are other criteria that have been studied in the touchdown bearing model. [3, pp. 406-413; 11, pp. 53-61; 12 pp. 154-163; 13, pp. 253-263.]

High contact stress between the ball and raceway of bearing degrades the life time of the bearing. The localized deformation and fracture fatigue are the consequence of the contact stress [14, p. 266]. The literature review on the contact stress in bearing shows that Hertzian contact model is the analytical method that can be applied for determining the contact stress and life time of the ball bearing and gears [1, pp. 604-605; 2, p. 694; 5, p. 243; 14, p. 266; 15, p.205].

In the literature, FEM have been proposed to explain the strain-stress distribution of the contact surfaces [14, pp. 267-269]. The accuracy of the results for both analytical and numerical method for calculating contact stress highly depends on the calculation of the loads exerted on the contact surfaces. Calculation of this load requires prior knowledge in the rotor dynamic and bearing model. Rolling contact stress is also imperative part of the analysis of the railroad industry and several studied has been done to model the contact stress and fatigue in railroad industry [16, pp. 985-997]. The effect of both surface and subsurface stress have been also considered to model the rolling contact fatigue in railroad industry [17, pp. 899-909].

However, few publications can be found that discussed about the issue of life and stress analysis in touchdown bearings [15, pp. 203-209; 18, p. 031101.1]. Sun [15, p. 205] utilized the Hertzian contact model to estimate the fatigue life of the touchdown bearing in AMB of energy storage flywheel. These studies include one dimensional thermal model to demonstrate thermal growth in bearing parts. The results obtained by Sun [15, p. 209] indicate that by selecting proper damper and decreasing the temperature of the touchdown bearing, the fatigue life of touchdown bearing will be increased. Furthermore, Lee and Palazzolo [18, p. 031101.14] used rain flow analysis to predict the life time of touchdown bearing and they suggested that by decreasing the air gap in touchdown bearing, reducing the friction between the rotor and inner race in the dropdown event and modifying the support condition (by decreasing the stiffness and enhancing the damping of supports) the life time of the touchdown bearing can be increased. Helfert [19, pp. 10-15] investigated the contact of the rotor on the touchdown bearing during the dropdown. He implemented the video recording tool to capture the acceleration and the contact of the rotor on the touchdown bearing.

1.2 Research problem

In the dropdown event, the rotor impacts the bearing in several points of the touchdown bearing and the bearing experiences high stress. Evaluating the stress level in the dropdown is an essential requirement for estimating the life time of the touchdown bearing. It is challenging to obtain the stress that is a consequent of the contact in an infinitesimal area between ball and bearing race. Furthermore, calculation of the stress in touchdown bearing requires detailed investigation of the rotor dropdown. Therefore, several studies attempted to simulate the dropdown. Moreover, calculation of the normal contact force and applying the conventional method for the stress analysis are other obstacles in obtaining the stress in touchdown bearing.

1.3 Objectives and restrictions

The main purpose of this study is to determine the stress level in the touchdown bearing of the AMB system in the dropdown. During the dropdown of the rotor on touchdown bearing, the ball might contact both inner race and outer race. Providing the model which can determine the contact stress both for ball-inner race and ball-outer race requires the more complicated model of the bearing which includes the high speed effect (improved model [5, pp. 247-249]). Previous studies indicated that the contact stress between the ball and inner race is higher than the contact between the ball and outer race [20, p.438]. The author´s attention was concentrated on obtaining the stresses in the first contact. The results of current study presents the maximum contact stress and normal force between the each ball and inner race. The accuracy of the model is highly dependent on the calculation of the penetration of the ball on the inner race and the initial value for the relative displacement of the rotor with respect to the bearing.

1.4 Research methodology

This research focuses on calculating the contact stress in the first contact of the rotor and touchdown bearing. For this purpose, current work can be divided in to four steps. First, the model for the rotor will be described. Second, the principal of theory of elasticity will be applied to demonstrate the general model for contact stress. Third, the relative displacement of the rotor bearing in the dropdown is extracted with the help of the RoBedyn (Rotor-Bearing Dynamics tool box for Matlab) that is developed in the laboratory of Machine Dynamic of the LUT (Lappeenranta University of Technology). This information, will be used to obtain the deformation of the ball on inner race, normal force and contact stress of the desired rotor. Finally, the normal force and maximum normal stress for each ball will be calculated.

## 2 MODELING OF THE STRESSES IN TOUCHDOWN BEARING

This study applies the Hertzian contact stress model to obtain the stresses in touchdown bearing. Figure 2.1 features the schematic of the rotor bearing model in AMB. During the normal operation the rotor is suspended in the AMBs and in the dropdown event the rotor is carried out by two touchdown bearings. The sensors shown in this figure detect the displacement of the rotor. In this study, the outer ring of the touchdown bearing is rigidly connected to the bearing housing. In this model, by applying the spring-damper system the bearing housing is attached to the ground. [1, pp. 608-609.] The support properties will be modeled with the help of spring damper system. This model will be a fundamental for determining the stresses in touchdown bearing. The first section of this chapter provides information about modeling of the rotor. Section, 2.2 is devoted to model the contact between ball and race. Section 2.3 describes how the theory of elasticity can be applied for modeling of the bearing. Then the normal force will be obtained from the model for the ball bearing (section 2.4-5). The last part of this chapter demonstrates the maximum Hertzian stress to obtain the stress in touchdown bearing.
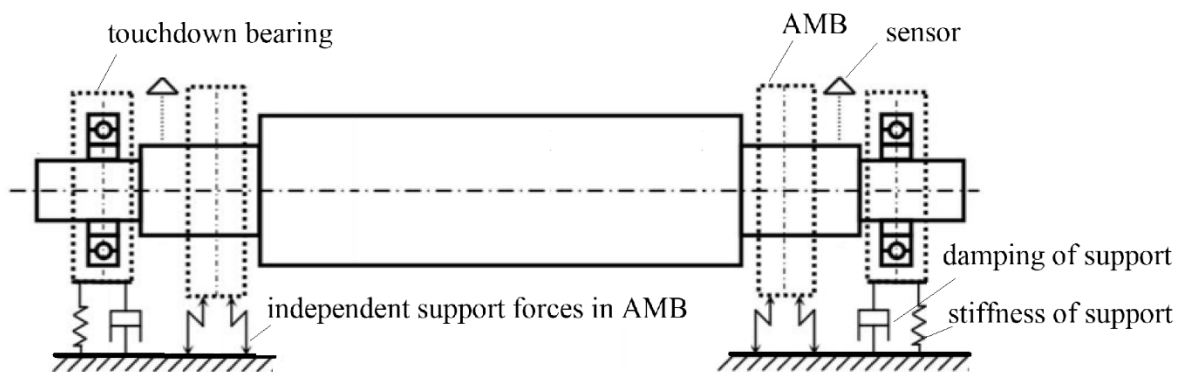


**Figure 2.1.** Schematic of the rotor bearing model in AMB [Mod. 21, p. 609]

2.1 Modeling of the rotor

In the literature, several researches have been done to explain the stability and natural frequency of the rotor [1, pp. 610-613; 4, pp. 167-388]. The simplification used in the traditional approach of the rotor dynamic system makes that the nonlinearities like the bearing clearance that is required for modeling the touchdown bearing cannot be directly considered in the model. Applying the flexible multibody dynamic method helps that aforementioned drawback and also other nonlinearities like waviness of the bearing ring can be simulated. Sopanen et al. [21, pp. 54-57] used this method to model super harmonic vibration of the tube roll in paper machine industry. However, this method often requires modal synthesis to reduce computational burden and time.

Current study applies the FEM for the rotor studied by Kärkkäinen [22, pp. 21-33]. In the FEM, the inertia and stiffness properties of the body can be taken into account. Above study concentrated on the lateral vibration and therefore the axial and torsional degrees of freedom are not considered in the element. In this model, the angular rotational speed of rotor, $\Omega$, is considered to be constant. The beam element is described by two nodes where each node has two translation $(u, v)$ and two rotational $(\theta_u, \theta_v)$ degrees of freedom (see Figure 2.2 (a)).



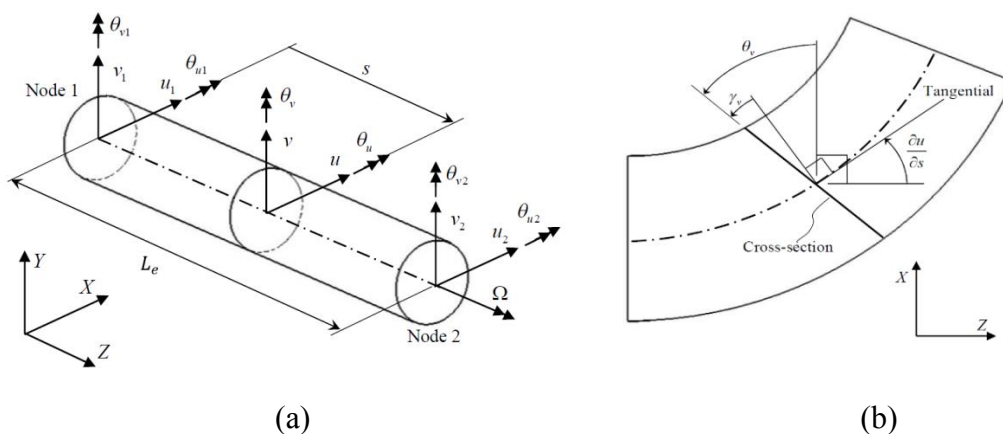(a)                                                                (b)

**Figure 2.2.** The finite element model of the beam [Mod. 22, pp. 23-24].

The vector of generalized coordinate for the element is given by [22, p. 22]:

$$\mathbf{q}^e = [u_1 \quad v_1 \quad \theta_{u1} \quad \theta_{v1} \quad u_2 \quad v_2 \quad \theta_{u2} \quad \theta_{v2}]^T \tag{2.1}$$

where subscripts 1, 2 defines degrees of freedom at node 1 (0,0) and node 2 ($L_e$,0), respectively. In Figure 2.2 (a), $L_e$ is length of the element. $u$ and $v$ can be defined by applying third order polynomial expansion given in equation (2.2) [22, p. 22].

$$\begin{bmatrix} u \\ v \end{bmatrix} = \begin{bmatrix} a_0 + a_1 s + a_2 s^2 + a_3 s^3 \\ b_0 + b_1 s + b_2 s^2 + b_3 s^3 \end{bmatrix} \tag{2.2}$$

where $s$ is the longitudinal coordinate depicted in Figure 2.2 (a). In equation (2.2) $a_0, \dots, a_3$ and $b_0, \dots, b_3$ are polynomial coefficients that can be defined by applying the Timoshenko beam theory in the cross section of the beam element. Equation (2.3) defines the relation between the slope of displacement in the beam cross section shown in Figure 2.2 (b), shear strain ($\gamma_u, \gamma_v$) and ($\theta_u, \theta_v$) [22, p. 23].

$$\frac{\partial u}{\partial s} = \theta_v - \gamma_v$$
$$\frac{\partial v}{\partial s} = \theta_u - \gamma_u \tag{2.3}$$

The angles $\gamma_u, \gamma_v$ are assumed to be constant in across the beam element. The force equilibrium for element can be expressed as follows [22, p. 24]:

$$\frac{\partial M}{\partial s} - V = 0 \quad , \quad M = -EI \frac{\partial \theta}{\partial s} \tag{2.4}$$

where $M$ and $V$ are moment and shear force in the cross section of the element. $E$ represents the modulus of elasticity and $I$ is moment of inertia. By substituting the shear force $V = K_s G A^* \gamma$ in equation (2.4) the force equilibrium can be rewritten as [22, p. 24]:

$$-EI \frac{\partial^2 \theta_u}{\partial s^2} - K_s G A^* \gamma_u = 0$$
$$-EI \frac{\partial^2 \theta_v}{\partial s^2} - K_s G A^* \gamma_v = 0 \tag{2.5}$$

where $K_s$ is shear correction factor, $G$ is shear modulus and $A^*$ is cross section of the beam element. Then, applying equation (2.2) and (2.3), the below relation will exist between the coefficients of the polynomial and the second derivative of the element rotation.

$$\frac{\partial^3 u}{\partial s^3} = \frac{\partial^2 \theta_v}{\partial s^2} = 6a_3 \quad , \qquad \frac{\partial^3 v}{\partial s^3} = \frac{\partial^2 \theta_u}{\partial s^2} = 6b_3 \tag{2.6}$$

Substituting (2.6) in (2.5) yields:

$$\gamma_u = -\frac{6EIb_3}{K_sGA^*}$$

$$\gamma_v = -\frac{6EIa_3}{K_sGA^*}$$

(2.7)

Then, by implementing equation (2.2), (2.3) and (2.7), $\theta_u$, $\theta_v$ can be defined as follows:

$$\theta_u = b_1 + 2b_2s + \left(3s^2 + \frac{6EI}{K_sGA^*}\right)b_3$$

$$\theta_v = a_1 + 2a_2s + \left(3s^2 + \frac{6EI}{K_sGA^*}\right)a_3$$

(2.8)

The coefficient in the polynomial can be determined by inserting the following boundary conditions in the polynomial approximation.

$$
\begin{aligned}
u(0) &= u_1 & , & & u(L_e) &= u_2 \\
v(0) &= v_1 & , & & v(L_e) &= v_2 \\
\theta_u(0) &= \theta_{u1} & , & & \theta_u(L_e) &= \theta_{u2} \\
\theta_v(0) &= \theta_{v1} & , & & \theta_v(L_e) &= \theta_{v2}
\end{aligned}
$$

(2.9)

Now, the shape function matrix ($\mathbf{N}(s)$) can be determined with the help of above polynomials and the vector of generalized coordinates given in equation (2.1) [22, p. 25].

$$\begin{bmatrix} u(s) \\ v(s) \\ \theta_u(s) \\ \theta_v(s) \end{bmatrix} = \mathbf{N}(s)\mathbf{q}^e = \begin{bmatrix} \mathbf{N}_T(s) \\ \mathbf{N}_R(s) \end{bmatrix}\mathbf{q}^e$$

(2.10)

In this work, the subscripts $T$, $N$ are attributed to the translational and rotational, respectively. The shape function matrix will be used to obtain the mass matrix and stiffness matrix in the equation of the motion of the rotor. The Lagrangian equation can be implemented to demonstrate the equation of the motion of the rotor as follows:

$$\frac{d}{dt}\left(\frac{\partial L}{\partial \dot{\mathbf{q}}}\right) - \left(\frac{\partial L}{\partial \mathbf{q}}\right) = \boldsymbol{Q}_e$$

(2.11)

where $L$ is the difference between the kinetic and potential energy of the system. $\boldsymbol{Q}_e$ is the vector of externally applied forces. The total kinetic energy ($T$) is sum of the translation ($T_T$) and rotational ($T_R$) kinetic energy of element [22, p. 27].

$$T = T_T + T_R$$

(2.12)

where

$$T_T = \frac{1}{2}\rho A^* \int_0^L (\dot{u}^2 + \dot{v}^2)\, ds \tag{2.13}$$

$$T_R = \frac{1}{2}\int_0^L \left(I_d\left(\dot{\theta}_u^{\,2} + \dot{\theta}_v^{\,2}\right) + I_p\Omega(\dot{\theta}_u\theta_v - \dot{\theta}_v\theta_u) + I_p\Omega^2\right) ds \tag{2.14}$$

where $\rho$ is density of element and $\dot{u}$, $\dot{v}$ are time derivative of displacement. It should be noted that the vector of generalized coordinate will change by time. The $I_p$ and $I_d$ (for circular cross section, $I_p = 2I_d$) are polar and diametric moment of inertia of element, respectively. In equation (2.14), the product of the moment of inertia, rotation angle and the angular velocity of element $(I_p\Omega\theta_v, I_p\Omega\theta_u)$ is the gyroscopic moments. By applying the shape function the mass matrix ($\mathbf{M}$) can be expressed by translational ($\mathbf{M}_T^e$) and rotational ($\mathbf{M}_R^e$) term [22, pp. 28-29]:

$$\mathbf{M}_T^e = \rho A^* \int_0^L \mathbf{N}_T^T\mathbf{N}_T\, ds$$
$$\mathbf{M}_R^e = \rho A^* \int_0^L \mathbf{N}_R^T\mathbf{N}_R\, ds \tag{2.15}$$

In addition, the gyroscopic matrix ($\mathbf{G}^e$) and intermediate gyroscopic matrix ($\mathbf{g}^e$) can be given by [22, p. 29]:

$$\mathbf{G}^e = -2\mathbf{g}^e = 2I_d \int_0^L \mathbf{N}_R^T \begin{bmatrix} 0 & 1 \\ -1 & 0 \end{bmatrix} \mathbf{N}_R\, ds \tag{2.16}$$

Therefore, the kinetic energy can be rewritten as [22, p. 28]:

$$T = \frac{1}{2}\dot{\mathbf{q}}^{eT}(\mathbf{M}_T^e + \mathbf{M}_R^e)\dot{\mathbf{q}}^e + \Omega\mathbf{q}^{eT}\mathbf{g}^e\dot{\mathbf{q}}^e \tag{2.17}$$

The strain energy of element ($U$) is sum of the elastic energy related to bending and shear deformation and is given by [22, p. 29]:

$$U = \frac{1}{2}\int_0^L \left( EI\left(\left(\frac{\partial\theta_u}{\partial s}\right)^2 + \left(\frac{\partial\theta_v}{\partial s}\right)^2\right) + K_sGA^*(\gamma_u^2 + \gamma_v^2) \right) ds \tag{2.18}$$

Equation (2.19) expresses the bending ($\mathbf{K}_b^e$) and shear ($\mathbf{K}_s^e$) stiffness matrix in terms of $\mathbf{N}_T$ and $\mathbf{N}_R$ [22, p. 29].

$$\mathbf{K}_b^e = EI \int_0^L \left(\frac{\partial \mathbf{N}_R}{\partial s}\right)^T \left(\frac{\partial \mathbf{N}_R}{\partial s}\right) ds$$

$$\mathbf{K}_s^e = K_s G A^* \int_0^L \left(\frac{\partial \mathbf{N}_T}{\partial s} + \mathbf{N}_R\right)^T \left(\frac{\partial \mathbf{N}_T}{\partial s} + \mathbf{N}_R\right) ds \qquad (2.19)$$

Thus, the strain energy can be rewritten as [22, p. 29]:

$$U = \frac{1}{2}\mathbf{q}^{eT}(\mathbf{K}_b^e + \mathbf{K}_s^e)\mathbf{q}^e \qquad (2.20)$$

Then, by applying the Lagrangian equation (2.11), the equation of motion can be obtained by [22, p. 30]:

$$\mathbf{M}\ddot{\mathbf{q}} + (\mathbf{C} + \Omega\mathbf{G})\dot{\mathbf{q}} + (\mathbf{K} + \dot{\Omega}\mathbf{G})\mathbf{q} = \Omega^2\mathbf{Q}_1 + \dot{\Omega}\mathbf{Q}_2 + \mathbf{F} \qquad (2.21)$$

where, $\mathbf{C}$ is the damping matrix, $\mathbf{F}$ is the vector of externally applied force. $\mathbf{Q}_1$ and $\mathbf{Q}_2$ are force vectors describing the mass unbalance of the rotor. The derivation of $\Omega$ at constant speed is equal to zero. Therefore, the equation of motion is given by [22, p. 31]:

$$\mathbf{M}\ddot{\mathbf{q}} + (\mathbf{C} + \Omega\mathbf{G})\dot{\mathbf{q}} + \mathbf{K}\mathbf{q} = \Omega^2\mathbf{Q}_1 + \mathbf{F} \qquad (2.22)$$

Although above equation can be solved by integration with respect to the time, but due to large number of equations that are coupled together the solution is computationally time demanding. For solving above equations, the modal synthesis can be applied to reduce the number of equation. In modal synthesis, the deformation of the element considered to be linear and it can be described in terms of modal coordinate. [22, pp. 31-32.]

$$\mathbf{q} = \mathbf{\Phi}\mathbf{P} \qquad (2.23)$$

where, $\mathbf{\Phi}$ and $\mathbf{P}$ are mode shape matrix and vector of modal coordinate. As the modes with lower frequency have considerable effect in the behavior the of system, by ignoring the mode related to the higher frequency the number of degrees of freedom can be reduced and the results still will have acceptable accuracy. Substituting the reduced matrix in equation (2.22), yields [22, p. 33]:

$$\mathbf{\Phi}^T\mathbf{M}\mathbf{\Phi}\ddot{\mathbf{P}} + (\mathbf{\Phi}^T\mathbf{C}\mathbf{\Phi} + \Omega\mathbf{\Phi}^T\mathbf{G}\mathbf{\Phi})\dot{\mathbf{P}} + (\mathbf{\Phi}^T\mathbf{K}\mathbf{\Phi} + \dot{\Omega}\mathbf{\Phi}^T\mathbf{G}\mathbf{\Phi})\mathbf{P} = \mathbf{\Phi}^T\mathbf{F}_{\text{tot}} \quad (2.24)$$

where, $\mathbf{F}_{\text{tot}}$ is a vector of the sum of the externally applied forces. Then, by performing the eigenvalue analysis and modal solution, the relative displacement of the rotor will be obtained. The information about the relative position of the rotor with respect to the bearing is required for modeling the bearing which will be described in section 2.5.

2.2 Model for the contact between the ball and inner race

In order to calculate the stress in the touchdown bearing, the normal force and the contact area between the ball and inner race should be known. It is difficult to find the stress in an small contact area between the ball and inner race (Figure 2.3). To solve this issue, many researches have been done to demonstrate either the contact between ball and inner race (point contact) or between the roller and inner race (line contact) [23, pp. 163-164].
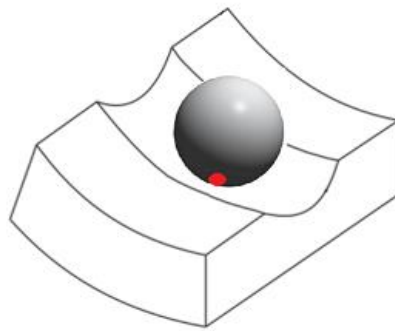


**Figure 2.3.** Point contact between ball and inner race.

For several years significant effort has been made to study the surface stress. In 1892, Boussinesq proposed equation (2.25) to solve the radial stress of semi-infinite body depicted in Figure 2.4. He used the polar coordinate $(r, \theta)$ and assumed there is no shear stress on the surface. [23, p. 142.]

$$\sigma_r = -\frac{2Q\cos\theta}{\pi r} \tag{2.25}$$
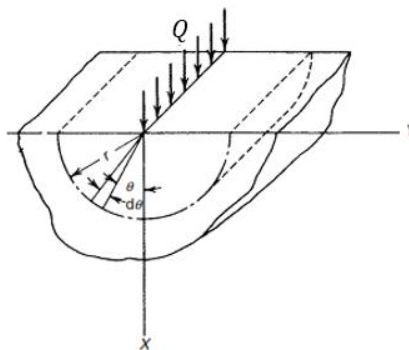


**Figure 2.4.** Semi infinitive body in Boussineq model [Mod. 23, p. 142].

The problem with this approach is that for the given value of normal force ($Q$), if the radius ($r$) approaches zero, the radial stress ($\sigma_r$) will be infinitive. Later, Hertz postulated the infinitesimal elliptic contact area rather than point contact or line contact which mitigates the problem of infinitive stress. He presumed that deformation occurs in the elastic region and the load is normal to the surface and there is no shear stress. In addition, he considered that the dimensions of the contact area are smaller than other dimensions of body and in the contact region, the radius curvature is considerably higher than other dimensions of the contact area. [23, p. 142.] This study, applies Hertzian contact model to obtain the stress in touchdown bearing. The principal of the Hertzian contact stress will be demonstrated in the following section.

2.3 Implementation of theory of elasticity for modeling the Hertzian contact model

In 1896, Hertz established a solution based on the theory of elasticity for the local stress of two bodies that have a point contact. Later, this method was known as Hertzian stress. Let us first obtain the force balance in $x$-direction on the small cube depicted in Figure 2.5. It is assumed that no body force is imposed to the cube. [23, p. 139.]
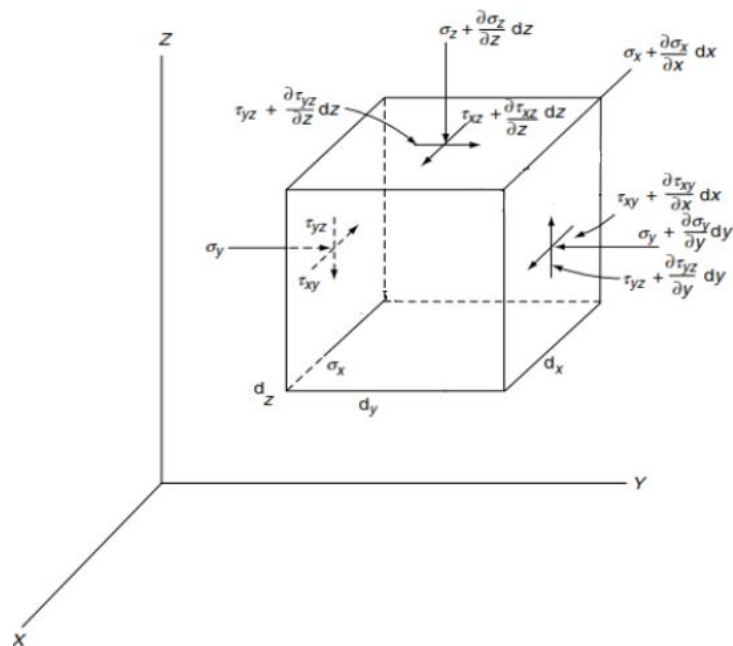


**Figure 2.5.** Normal and shear stress on cube [Mod. 23, p. 139].

$$\sigma_x dzdy + \tau_{xy} dxdz + \tau_{xz} dxdy - \left(\sigma_x + \frac{\partial \sigma_x}{\partial x} dx\right) dzdy$$

$$- \left(\tau_{xy} + \frac{\partial \tau_{xy}}{\partial y} dy\right) dxdz - \left(\tau_{xz} + \frac{\partial \tau_{xz}}{\partial z} dz\right) dxdy = 0 \tag{2.26}$$

where $\sigma_x$ is normal stress in $x$-direction, $\tau_{xy}$ and $\tau_{xz}$ are shear stress in $xy$-plane and $xz$-plane, respectively. By mathematical manipulation of equation (2.26) and also applying similar procedure for $y$ and $z$-direction, the force balance can be written as [23, pp. 139-140]:

$$\frac{\partial \sigma_x}{\partial x} + \frac{\partial \tau_{xy}}{\partial y} + \frac{\partial \tau_{xz}}{\partial z} = 0$$

$$\frac{\partial \sigma_y}{\partial y} + \frac{\partial \tau_{xy}}{\partial x} + \frac{\partial \tau_{yz}}{\partial z} = 0 \tag{2.27}$$

$$\frac{\partial \sigma_z}{\partial z} + \frac{\partial \tau_{xz}}{\partial x} + \frac{\partial \tau_{yz}}{\partial y} = 0$$

The equation that describes normal strain ($\varepsilon$) in $x$, $y$ and $z$-direction is as follows [23, p. 140]:

$$\varepsilon_x = \frac{\partial u^*}{\partial x}$$

$$\varepsilon_y = \frac{\partial v^*}{\partial y} \tag{2.28}$$

$$\varepsilon_z = \frac{\partial w^*}{\partial z}$$

where $u^*$, $v^*$ and $w^*$ are deformations in $x$, $y$ and $z$-direction. If the deformation is not perpendicular to axis, the element will have a relative rotation and the rotational strain ($\gamma$) that can be expressed by [23, p. 140]:

$$\gamma_{xy} = \frac{\partial u^*}{\partial y} + \frac{\partial v^*}{\partial x}$$

$$\gamma_{xz} = \frac{\partial u^*}{\partial z} + \frac{\partial w^*}{\partial x} \tag{2.29}$$

$$\gamma_{yz} = \frac{\partial v^*}{\partial z} + \frac{\partial w^*}{\partial y}$$

The Hooke's low describes that in elastic material, $\sigma$ has linear relation with $\varepsilon$ [23, p. 140]:

$$\varepsilon = \frac{\sigma}{E} \tag{2.30}$$

Moreover, the strain in the $y$ and $z$-direction are proportional to $x$-direction with the Poisson's ratio $(v)$ [23, p. 140]:

$$\varepsilon_x = \frac{\sigma_x}{E}$$
$$\varepsilon_y = -v\frac{\sigma_x}{E} \tag{2.31}$$
$$\varepsilon_z = -v\frac{\sigma_x}{E}$$

The superposition principal postulates that the strain in each axis is affected by stress in other axes. Therefore equation (2.31) can be rewritten as [23, pp. 140-141]:

$$\varepsilon_x = \frac{1}{E}\left[\sigma_x - v(\sigma_y + \sigma_z)\right]$$
$$\varepsilon_y = \frac{1}{E}\left[\sigma_y - v(\sigma_x + \sigma_z)\right] \tag{2.32}$$
$$\varepsilon_z = \frac{1}{E}\left[\sigma_z - v(\sigma_x + \sigma_y)\right]$$
$$\varepsilon = \varepsilon_x + \varepsilon_y + \varepsilon_z$$

In addition, equation (2.33) exists between $G$ and $E$ [23, p. 141]:

$$G = \frac{E}{2(1+v)} \tag{2.33}$$

The total strain is the sum of the strain in axes. Thus, the following equation is obtained [23, p. 141]:

$$\sigma_x = 2G\left(\frac{\partial u^*}{\partial x} + \frac{v}{1-2v}\varepsilon\right)$$
$$\sigma_y = 2G\left(\frac{\partial v^*}{\partial y} + \frac{v}{1-2v}\varepsilon\right) \tag{2.34}$$
$$\sigma_z = 2G\left(\frac{\partial w^*}{\partial z} + \frac{v}{1-2v}\varepsilon\right)$$

Then, the following set of equation can be obtained by differentiation of $\varepsilon, \gamma$ and substituting them in equation (2.27) [23, p.141]:

$$\nabla^2 u^* + \frac{1}{1-2v}\frac{\partial \varepsilon}{\partial x} = 0$$

$$\nabla^2 v^* + \frac{1}{1-2v}\frac{\partial \varepsilon}{\partial y} = 0 \tag{2.35}$$

$$\nabla^2 w^* + \frac{1}{1-2v}\frac{\partial \varepsilon}{\partial z} = 0$$

where

$$\nabla^2 = \frac{\partial^2}{\partial x^2} + \frac{\partial^2}{\partial y^2} + \frac{\partial^2}{\partial z^2} \tag{2.36}$$

Finally, above set of equations should be solved to obtain the strain. Accordingly, the stress can defined. This solution will be a fundamental for deriving the maximum contact stress in the bearing that will be demonstrated in the section 2.6.

Hertz used the dimensionless parameters, the dimensionless deformation and the arbitrary function to solve the stress. By introducing the arbitrary fixed length ($l$), the principal directions distances ($x, y, z$) are converted to the dimensionless forms as equation (2.37). [23, p. 143.]

$$X = \frac{x}{l}$$

$$Y = \frac{y}{l} \tag{2.37}$$

$$Z = \frac{z}{l}$$

These dimensionless parameters ($X, Y, Z$) are used in defining the arbitrary functions named $U^*$ and $V^*$ that satisfy below condition [23, p. 143]:

$$\nabla^2 U^* = 0$$

$$\nabla^2 V^* = 0 \tag{2.38}$$

Then, by applying the arbitrary length of $c$, the dimensionless form of $u^*$, $v^*$ and $w^*$ can be written as [23, p. 143]:

$$\frac{u^*}{c} = \frac{\partial U^*}{\partial X} - Z\frac{\partial V^*}{\partial X} \tag{2.39}$$

$$\frac{v^*}{c} = \frac{\partial U^*}{\partial Y} - Z\frac{\partial V^*}{\partial Y}$$

$$\frac{w^*}{c} = \frac{\partial U^*}{\partial Z} - Z\frac{\partial V^*}{\partial Z} + V^*$$

In above equation $\frac{u^*}{c}$, $\frac{v^*}{c}$ and $\frac{w^*}{c}$ are dimensionless form of deformation. These arbitrary lengths $(l, c)$ and arbitrary function $(U^*)$ are related together with the following equation [23, p. 143].

$$\frac{l\varepsilon}{c} = -2\frac{\partial^2 U^*}{\sigma Z^2} \tag{2.40}$$

These hypothesis are established on a combination of intuitive and experience. These dimensionless deformations and dimensionless parameters are combined with equation (2.29), (2.32), (2.34) and (2.35). Thus, the normal and shear stress can be expressed as the following [23, pp. 143-144]:

$$
\begin{aligned}
\frac{\sigma_x}{\sigma_o} &= Z\frac{\partial^2 V^*}{\partial^2 X} - \frac{\partial^2 U^*}{\partial^2 X} - 2\frac{\sigma V^*}{\sigma Z} \\
\frac{\sigma_y}{\sigma_o} &= Z\frac{\partial^2 V^*}{\partial^2 Y} - \frac{\partial^2 U^*}{\partial^2 Y} - 2\frac{\sigma V^*}{\sigma Z} \\
\frac{\sigma_z}{\sigma_o} &= Z\frac{\partial^2 V^*}{\partial^2 Z} - \frac{\sigma V^*}{\sigma Z} \\
\frac{\tau_{xy}}{\sigma_o} &= Z\frac{\partial^2 V^*}{\sigma X \sigma Z}
\end{aligned}
\tag{2.41}
$$

where

$$\sigma_o = -\frac{2Gc}{l} \tag{2.42}$$

$$U^* = (1 - 2v)\int_Z^\infty V^*(X, Y, Z, v)dv \tag{2.43}$$

$$V^* = \frac{1}{2}\int_{S_o}^\infty \frac{\left(1 - \frac{X^2}{\kappa^2 + S^2} - \frac{Y^2}{1 + S^2} - \frac{Z^2}{S^2}\right)}{\sqrt{(\kappa^2 + S^2)(1 + S^2)}}\kappa dS \tag{2.44}$$

and

$$\kappa = \frac{a}{b} \tag{2.45}$$

where $\sigma_o$ is stress at center of geometry, $S$ is principal stress, $S_o$ is the largest positive root of the equation 2.44. In equation (2.45), $\kappa$ is named as elliptic eccentricity parameter, $a$ and $b$ are semi-minor and semi-major axis of the elliptic area depicted in Figure 2.6. This elliptic area is created from the projection of the contact area. [23, p. 144.]
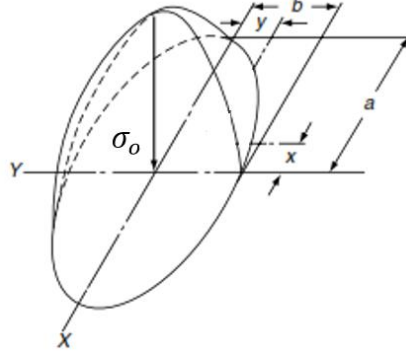


**Figure 2.6.** Stress in elliptical surface [Mod. 23, p. 149].

For modeling the contact stress, the area of ellipse ($\pi a b$) should be defined. $a$ and $b$ can be obtained with the help of dimensionless quantities, amount of force and material properties of the contact area. Let us introduce the supplementary quantity $F(\rho)$ [23, pp. 144-145]:

$$F(\rho) = \frac{(\kappa^2 + 1)\bar{\bar{\zeta}} - 2\bar{\bar{\xi}}}{(\kappa^2 - 1)\bar{\bar{\zeta}}} \tag{2.46}$$

where

$$\bar{\bar{\xi}} = \int_0^{\frac{\pi}{2}} \left[1 - \left(1 - \frac{1}{\kappa^2}\right)\sin^2\vartheta\right]^{-1/2} d\vartheta \tag{2.47}$$

$$\bar{\bar{\zeta}} = \int_0^{\frac{\pi}{2}} \left[1 - \left(1 - \frac{1}{\kappa^2}\right)\sin^2\vartheta\right]^{1/2} d\vartheta \tag{2.48}$$

where $\bar{\bar{\xi}}$, $\bar{\bar{\zeta}}$ are elliptical integral of first and second kind, correspondingly. $\bar{\bar{\xi}}$ and $\bar{\bar{\zeta}}$ are defined by auxiliary angle ($\vartheta$) and $\kappa$. By presuming the value for $\kappa$, the function $F(\rho)$ can be defined. The following dimensionless parameters ($a^*, b^*$ and $\delta^*$) are required to obtain the $a$, $b$ and deformation of the contact area ($\delta$) [23, p. 146].

$$a^* = \left(\frac{2\kappa^2\bar{\bar{\zeta}}}{\pi}\right)^{1/3} \tag{2.49}$$

$$b^* = \left(\frac{2\bar{\zeta}}{\pi\kappa}\right)^{1/3} \tag{2.50}$$

$$\delta^* = \frac{2\bar{\zeta}}{\pi}\left(\frac{\pi}{2\kappa^2\bar{\zeta}}\right)^{1/3} \tag{2.51}$$

Then $a$, $b$ and $\delta$ can be calculated as the following [23, pp. 145-146]:

$$a = a^*\left[\frac{3Q}{2\sum\rho}\left(\frac{(1-v_I^2)}{E_I} + \frac{(1-v_{II}^2)}{E_{II}}\right)\right]^{1/3} \tag{2.52}$$

$$b = b^*\left[\frac{3Q}{2\sum\rho}\left(\frac{(1-v_I^2)}{E_I} + \frac{(1-v_{II}^2)}{E_{II}}\right)\right]^{1/3} \tag{2.53}$$

$$\delta = \delta^*\left[\frac{3Q}{2\sum\rho}\left(\frac{(1-v_I^2)}{E_I} + \frac{(1-v_{II}^2)}{E_{II}}\right)\right]^{2/3}\frac{\sum\rho}{2} \tag{2.54}$$

where, the subscribes $I$ and $II$ are related to the material properties of the contact bodies (see Figure 2.7).
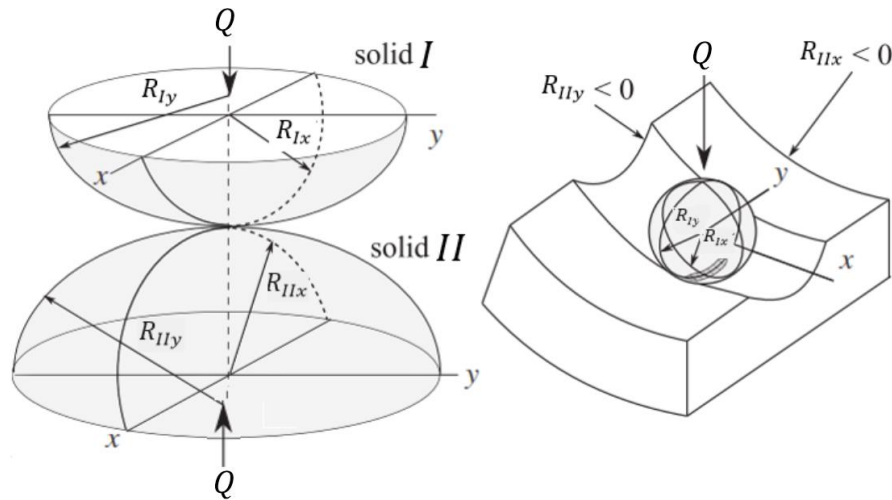


**Figure 2.7.** Modeling of the elliptical contact in the ball bearing [Mod. 5, p. 243].

The calculation of the maximum contact stress depends on the presumed value for $\kappa$ and the value of $\bar{\xi}$ and $\bar{\zeta}$. For this reason, several publications have been appeared in previous years documenting the model for contact parameter. In late of 20 [th] century, Greenwood [24, pp. 235-237] proposed a rough approximation model applying the effective radius of the contact

curvature ($R_e$) for calculating the contact stress. In this method $a$ and $b$ can be calculated straightforwardly. The equation that describes $R_e$ is as follows [24, p. 235]:

$$R_e = \left[ AB \left( \frac{A+B}{2} \right) \right]^{-1/3} \tag{2.55}$$

where

$$A = 1/R_x = 1/R_{Ix} + 1/R_{IIx} \tag{2.56}$$

$$B = 1/R_y = 1/R_{Iy} + 1/R_{IIy} \tag{2.57}$$

where $A$ and $B$ are inverses of the effective radius of curvature in $x$ and $y$-direction and they can be obtained from the radius of bodies $(R_{Ix}, R_{Iy})$, $(R_{IIx}, R_{IIy})$ through $x$ and $y$-axes ( see Figure 2.7). Greenwood [24, pp. 235-237] proposed the following approximation for the cases where the only ratio of $a$ and $b$ is required [24, p. 235].

$$\left( \frac{b}{a} \right) \sim \left( \frac{A}{B} \right)^{2/3} \tag{2.58}$$

Apart from this, he expressed the equation (2.59) for calculation of $a$ and $b$ [24, p. 235]. Another method for obtaining $a$ and $b$ was previously shown in equation (2.52) and (2.53).

$$a = \left( \frac{3\kappa^2 \bar{\bar{\xi}} QR}{\pi E^*} \right)^{1/3}, b = \left( \frac{3\bar{\bar{\xi}} QR}{\pi \kappa E^*} \right)^{1/3} \tag{2.59}$$

where

$$\frac{1}{E^*} = \frac{1 - \nu_I^2}{E_I} + \frac{1 - \nu_{II}^2}{E_{II}} \tag{2.60}$$

$E^*$ is equivalent modulus of elasticity and it is obtained by $\nu$ and $E$ of the body I and II. The integral form of $\bar{\bar{\xi}}$ was defined in equation (2.47). The $\kappa$, $\bar{\bar{\xi}}$ can be defined by the following approximation introduced by Brewe and Hamrock [25, pp. 485-487].

$$\kappa \approx 1.0339 \left( \frac{B}{A} \right)^{0.636} \tag{2.61}$$

$$\bar{\bar{\xi}} \approx 1.0003 + 0.5968 \left( \frac{A}{B} \right) \tag{2.62}$$

The drawback of above approximation is that for circular contact ($A = B$), the error of calculating $\kappa$ and $\bar{\bar{\xi}}$ are high (3.4% and 1.7%, respectively) [24, pp. 235-237]. Later, this

drawback was eliminated in the Hamrock and Brewe's model [26, pp. 171-177] that suggested the following equation:

$$\kappa \approx \left(\frac{B}{A}\right)^{2/\pi} \tag{2.63}$$

$$\bar{\xi} \approx 1 + \left(\frac{\pi}{2} - 1\right)\left(\frac{A}{B}\right) \tag{2.64}$$

Greenwood [24, pp. 235-237] validated his model with the industrial measurement. Furthermore, he compared his model with the two other models (The first model that is provided Brewe and Hamrock and second model given by Hamrock and Brewe). As can be seen in Figure 2.8, for $B/A \leq 25$ the error of calculating the maximum contact stress in three models is lower than 2%. When $2.5 \leq B/A \leq 22$, the error of Brewe and Hamrock is remarkably low. For $B/A \leq 5$ , the error of Greenwood's model as well as the model of Brewe and Hamrock is considerably low (0.2%). For circular contact the error of the Hamrock and Brewe model is almost zero while the Brewe and Hamrock gives high error. Greenwood noted that there are only few cases that the error should not exceed 3% and three models give reasonable results. [24, p. 236.] According to above discussion, the available approximation for elliptical contact are appropriate for investigating the contact of the ball on bearing race. In this study $\kappa$ is calculated by equation (2.61). The equation (2.62) is used to obtain $\bar{\xi}$. The $a$ and $b$ are obtained from equation (2.59).
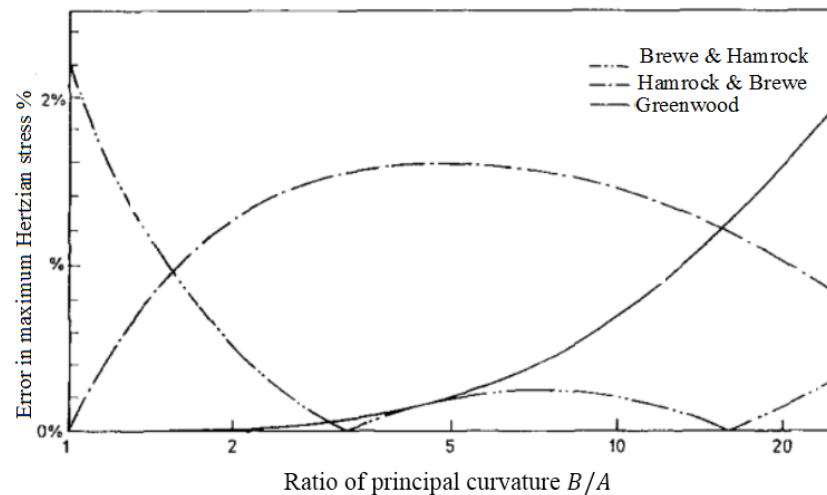


**Figure 2.8.** Comparison of errors in calculating the maximum Hertzian stress in the models provided by Greenwood, Brewe & Hamrock and Hamrock & Brewe [Mod. 24, p. 236].

2.4 Normal force in ball bearing

The literature on modeling of the ball bearing shows that for calculating the maximum Hertzian contact stress, the normal force between the contact area of the ball and races should be known ($Q$ in Figure 2.7). The equation that describes $Q$ as a function of total elastic deformation ($\delta_j^{tot}$) and total contact stiffness ($K_c^{tot}$) is as follows [1, p. 604; 2, p. 694; 5, p. 246]:

$$Q_i = K_c^{tot}\left(\delta_j^{tot}\right)^{3/2} \tag{2.65}$$

where the subscript $j$ refers to the contact between the ball number $j$ and inner race. The $K_c^{tot}$ can be defined by [1, p. 604]:

$$K_c^{tot} = \left(\left(\frac{1}{K_c^{in}}\right)^{2/3} + \left(\frac{1}{K_c^{out}}\right)^{2/3}\right)^{-3/2} \tag{2.66}$$

where $K_c^{in}$, $K_c^{out}$ are contact stiffness coefficients of the inner race and outer race, respectively. These coefficients can be obtained as the following [1, p. 604]:

$$K_c^{in,out} = \pi\kappa E^* \sqrt{\frac{R_e\bar{\xi}}{4.5\bar{\zeta}^3}} \tag{2.67}$$

Equation (2.54) represents an expression for determining the deformation between two contact bodies and the dynamic of the ball bearing is not included in this equation. Thus, for obtaining $\delta_j^{tot}$ it is not sufficient and supplementary model for computing the deformation in the ball bearings is essential and it will be explained in the following section.

2.5 Model for bearing

For many years, a considerable amount of literature has been published on the study of ball bearing. In recent years, some improvements have been achieved by modeling the defects in the bearing and considering proper usage of model complexity. It is possible to further improve the model for predicting the life of the touchdown bearing by implementing a more accurate model in the calculation of bearing load. With this goal, this work explores to apply an appropriate model for touchdown bearing.

In a recent paper by Kurvinen et al. [5. 243-249], two models for the ball bearing with cage is provided. The first model is established on the relative displacement and velocities between the races and the centrifugal forces and gyroscopic moment are not taken into account. The second model includes the externally applied forces, gyroscopic effect and centrifugal forces. For simplifying and reducing the number of degrees of freedom, they did not consider the friction torque, hydrodynamic film and the defects in the model. Both simplified and improved model apply the nonlinear Hertzian contact to calculate the contact force and deformation in bearing. In this section the first model will be discussed. Furthermore, available models for the bearing with cage can be a fundamental for describing the cageless bearing that is nominated for touchdown bearing [2, pp. 692-705]. The model for cageless bearing provided by Halminen et al. [2, pp. 692-705] the same as Kärkkäinen et al. [1, pp. 604-607] and Kurvinen et al. [5, pp. 243-246] is established on the relative displacement of the rotor with respect to the bearing and calculation of the deformation. This model for cageless bearing, the same as simplified model does not contain centrifugal force and gyroscopic effect.

In the simplified model described by Kurvinen et al. [5, pp. 243-246], the effect of the friction and hydrodynamic oil film as well as the defects are neglected. This model assumes that the bearing is in good manufacturing condition and there is no defect in the bearing. Figure 2.9 features the main dimensions and geometry of above model. In this Figure $d$ is ball diameter, $r_{in}$ and $r_{out}$ are radius of inner race and outer race, respectively. The pitch diameter, the distance from center of the inner race to the center of the ball ($d_m$), bearing diametric clearance ($c_d$), bore diameter ($d_s$), outer diameter of the bearing ($D_h$), diameter of inner race ($D_i$) and diameter of outer race ($D_o$) are determined from the bearing manufacturer data.
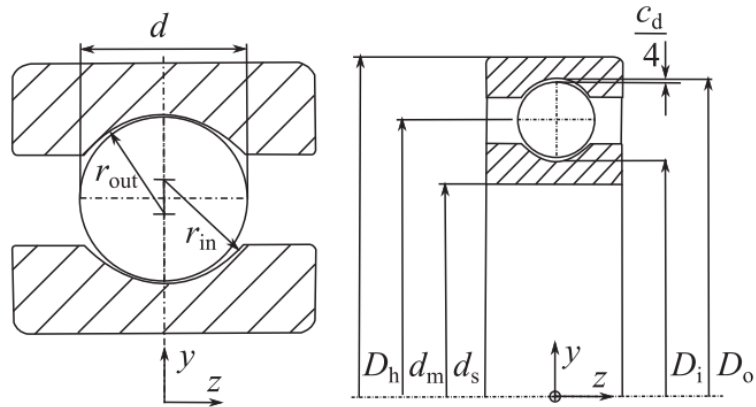
**Figure 2.9.** Dimensions used for simplified model [5, p. 244].

The forces and the moments in the ball bearing are achieved by computing the relative displacement of the ball and races. As shown in Figure 2.10, the displacement of the ball number $j$ in radial ($e_j^r$) and tangential ($e_j^t$) direction can be calculated by [5, p. 245]:

$$e_j^r = e_x\cos\beta_j + e_y\sin\beta_j$$
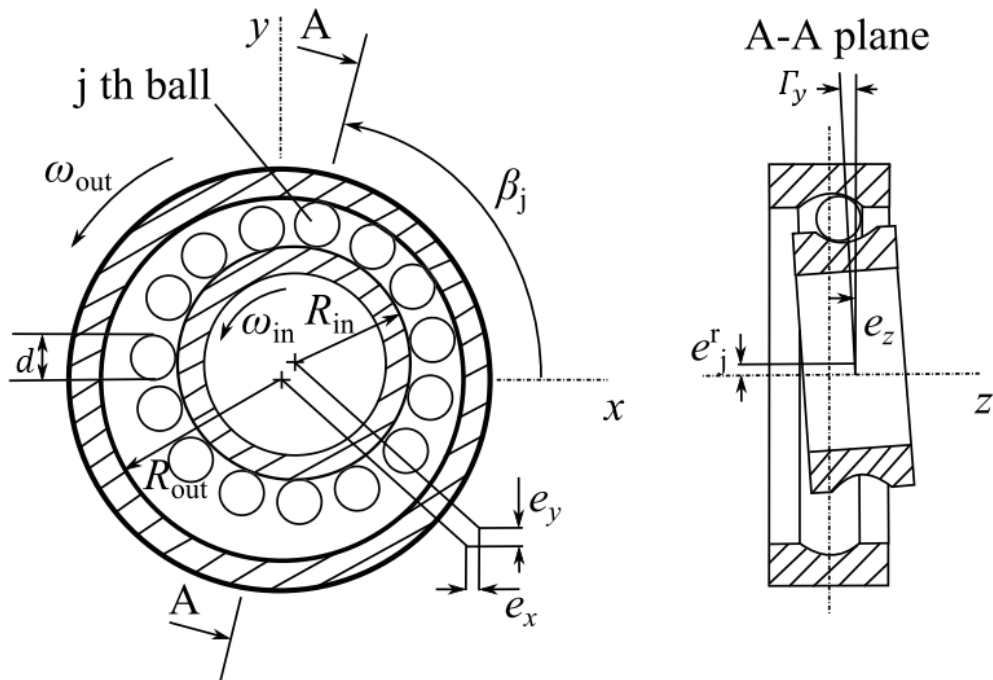$$e_j^t = e_z - (\Gamma_x\sin\beta_j + \Gamma_y\cos\beta_j)(R_{in} + r_{in})$$

$$(2.68)$$



**Figure 2.10.** Cross-section of the ball bearing [Mod. 5, p. 245].

In above equation, $e_x$, $e_y$ and $e_z$ describe the relative displacements along principal directions, $\Gamma_x$ and $\Gamma_y$ represent the angular misalignment of inner race in $x$ and $y$-direction. $\beta_j$ is azimuth angle (this angle shows the location of the ball $j$ among the total number of balls ($n$)) and it can be obtained by equation (2.69). [5, p. 245.]

$$\beta_j = \frac{2\pi(j-1)}{n} \tag{2.69}$$

The contact angle ($\varphi_j$) shown in Figure 2.11 is given by [5, p. 245]:

$$\varphi_j = \tan^{-1}\left(\frac{e_j^t}{R_{in} + r_{in} + e_j^r - R_{out} + r_{out}}\right) \tag{2.70}$$

where $R_{in}$ and $R_{out}$ are radius shown in Figure 2.10. Equation (2.71) represents the distance between inner race and outer race ($\acute{d}$) [5, p. 245].

$$\acute{d} = r_{out} + r_{in} - \frac{R_{in} + r_{in} + e_j^r - R_{out} + r_{out}}{\cos\varphi_j} \tag{2.71}$$
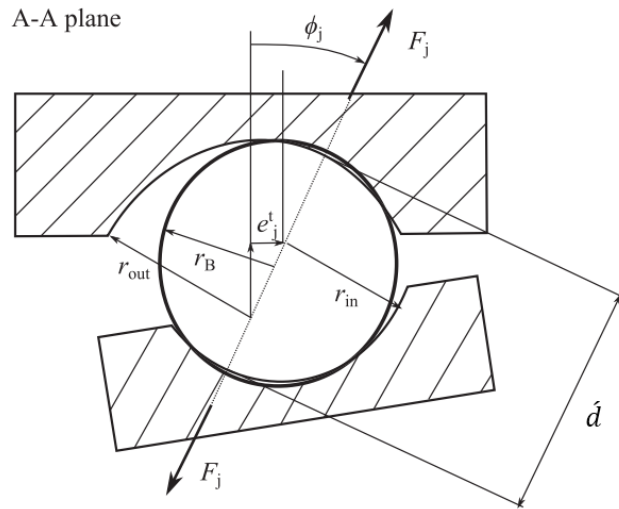


**Figure 2.11.** Ball bearing section view A-A [Mod. 5, p. 246].

where

$$R_{out} = \frac{d_m}{2} + \frac{c_d}{4} + r_b \tag{2.72}$$

and

$$R_{in} = d_m - R_{out} \tag{2.73}$$

In equation (2.72), $r_b$ is radius of the ball. Thus, the total deformation ($\delta_i^{tot}$), can be calculated by [5, p. 245]:

$$\delta_i^{tot} = 2r_b - \acute{d} \tag{2.74}$$

Kärkkäinen et al. [1, p. 605] provided a model for the bearing with cage which the oil film thickness is taken into account (see Figure 2.12). In their study, the same as the simplified model of Kurvinen et al. [5, pp. 243-247], the centrifugal force and the gyroscopic effect is neglected. Therefore, the total deformation described in equation (2.74) can be rewritten as [1, p. 605]:

$$\delta_i^{tot} = 2r_b + h_o^{in} + h_o^{out} - \acute{d} \tag{2.75}$$

where $h_o^{in}$, $h_o^{out}$ are oil film thickness between ball and races. It should be considered that the contact of the ball on the inner race compresses the inner race and the deflection will have positive value. Current study considers that the bearing does not require lubrication and the oil film thickness is ignored.
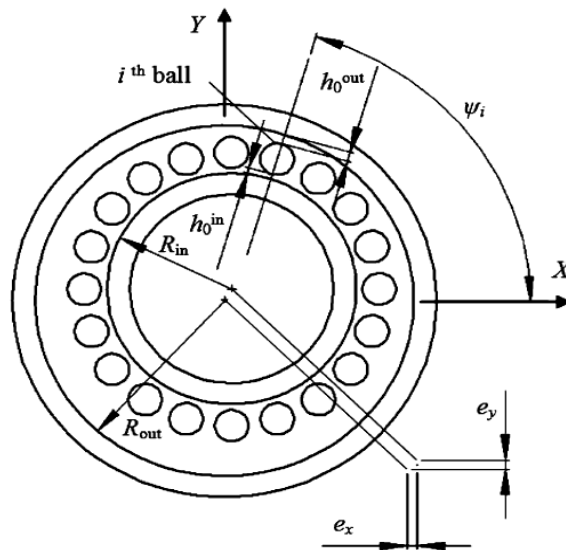


**Figure 2.12.** Cross section of the ball bearing including the oil film thickness [1, p. 605].

After the normal contact force is known from equation (2.65), the bearing forces $(Q_x, Q_y, Q_z)$ and the moments $(T_x, T_y)$ along $x$, $y$ and $z$ axis can be defined by the following equation [5, p. 246]:

$$
\begin{aligned}
Q_x &= -\sum_{j=1}^{n} Q_j \cos\varphi_j \cos\beta_j \\
Q_y &= -\sum_{j=1}^{n} Q_j \cos\varphi_j \sin\beta_j \\
Q_z &= -\sum_{j=1}^{n} Q_j \sin\varphi_j \\
T_x &= -\sum_{j=1}^{n} Q_j(R_{in} + r)\sin\varphi_j \sin\beta_j \\
T_y &= -\sum_{j=1}^{n} Q_j(R_{in} + r)\sin\varphi_j(-\cos\beta_j)
\end{aligned}
\tag{2.76}
$$

2.6 Maximum Hertzian stress

As previously mentioned at the geometric center of elliptic area the contact stress has maximum value ($\sigma_{max} = \sigma_o$). Hetrz introduced that the maximum contact stress can be calculated by [23, p. 148]:

$$
\sigma_{max} = \frac{3Q}{2\pi ab}
\tag{2.77}
$$

The stress in different point of the contact bodies can be obtained by [23, p. 148]:

$$
\sigma = \frac{3Q}{\pi ab}[1 - (x/a)^2 - (y/b)^2]^{1/2}
\tag{2.78}
$$

This method can also be a fundamental to obtain the subsurface stress in the bearing. The subsurface stress becomes important because the failure analysis revealed that in the surface fatigue failure initiated from the point under surface [23, p. 150].

# 3   NUMERICAL RESULTS

This chapter presents the numerical results for the simulation of the stresses in a touchdown bearing during the dropdown event. Section 3.1 provides information about the case study that has been modeled. Then, the stresses have been evaluated for three conditions (section 3.2-4). First, the stresses in the dropdown where the rotor rotates at zero rpm and the nominal bearing clearance is 1 μm. Second, dropdown at 9000 rpm with the bearing clearance equal to 1 μm. Third, the stress in the dropdown of the rotor at 9000 rpm and the bearing clearance increased to 5 μm.

## 3.1 Rotor under investigation

Current study applies Hertzian stress model to evaluate the stress on the touchdown bearing and the rotor depicted in Figure 3.1. During the dropdown, the rotor is carried out by two deep groove ball bearings that are located at 0.025 m from ends of the shaft. The main data for the simulation of the rotor is shown in Table 3.1. The dimension and material properties of the touchdown bearing are given in Table 3.2.
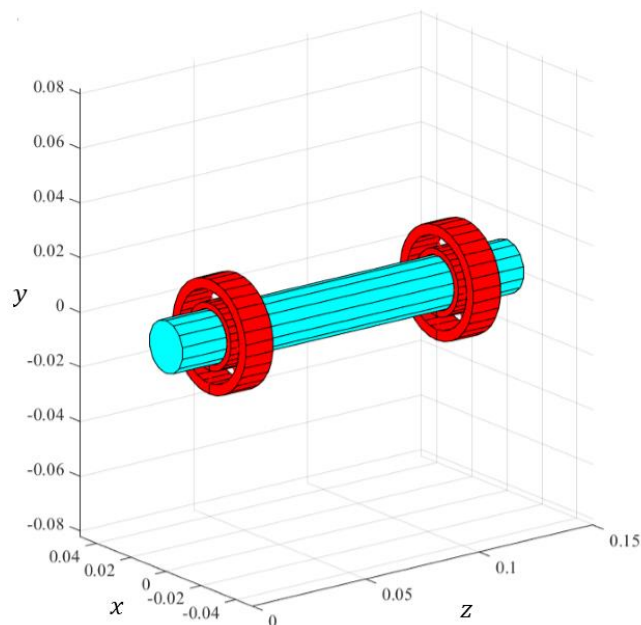


**Figure 3.1.** 3D plot of the rotor under investigation.

*Table 3.1. The main data for the simulation of the rotor dropdown.*

| Modulus of elasticity | 2.07e11 Pa |
|---|---|
| Material density | 7800 kg/m$^3$ |
| Poisson's ratio | 0.3 |
| Rotor diameter | 0.0194 m |
| Rotor length | 0.150 m |
| Support mass | 5 kg |
| Support stiffness | 2.5e8 N/m |
| Support damping | 2500 Ns/m |
| Diametric clearance between the race and rotor | 600 μm |

*Table 3.2. The dimension of the bearing.*

| Bearing damping coefficient | $C_b$ | 0.3 Ns/mm |
|---|---|---|
| Bearing diametric clearance | $c_d$ | 1 μm |
| Outer diameter | $D_h$ | 42.0 mm |
| Ball diameter | $d$ | 6.35 mm |
| Pitch Diameter | $d_m$ | 31.0 mm |
| Bore diameter | $d_s$ | 20.0 mm |
| Modulus of elasticity of ball | $E_b$ | 2.07e11 Pa |
| Modulus of elasticity of inner race | $E_i$ | 2.07e11 Pa |
| conformity ratio in inner race | $f_i$ | 0.52 |
| conformity ratio in outer race | $f_o$ | 0.52 |
| Number of balls | $n$ | 9 |
| Poisson's ratio of ball | $v_b$ | 0.3 |
| Width | $W$ | 12 mm |

Chapter two showed that the normal contact force depends on the deformation of the inner race in dropdown event. In order to calculate the deformation of inner race, the displacement of the bearing in $x$, $y$ and $z$-direction is required. These displacements ($e_x, e_y, e_z$) are extracted from the results of the previous study in the Laboratory of Machine Dynamic at LUT. The rotor dropdown is simulated by RoBeDyn (Rotor-Bearing Dynamics tool box for Matlab). This simulation package is developed by Laboratory of Machine Dynamic at LUT. Figure 3.2 shows the location of touchdown bearing in the FEM model of the rotor in RoBeDyn.
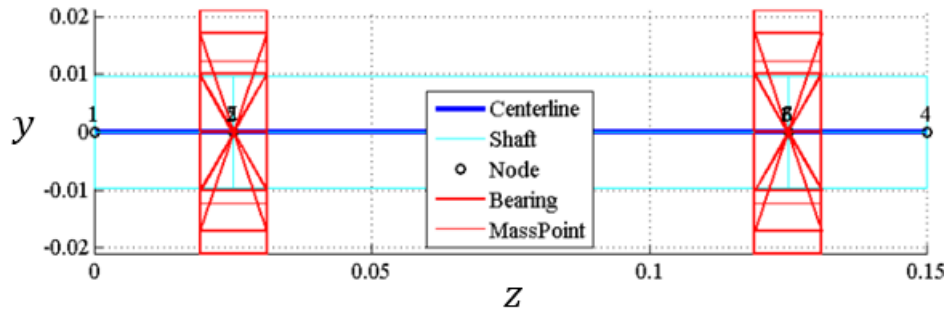
**Figure 3.2.** Position of the rotor in the finite element model of the rotor.

3.2 Stress in the dropdown of the rotor at zero rpm and 1 μm clearance

In the first case, the rotation speed of the rotor before dropdown is equal to zero rpm and the nominal bearing clearance is 1 μm. The dropdown is simulated for 0.025s. The displacement of the rotor in $y$-direction is shown in Figure 3.3. Figure 3.4 depicts the displacement of the bearing in whole dropdown simulation and it shows that when the dropdown happens at zero rpm, the bearing will have a small displacement of 2.151e-5 mm in $x$-direction at 0.0187 s and in the rest of simulation time remains at zero position. The displacement of the bearing in $y$-direction reveals at zero rpm, the rotor contacts the bearing two times, first at 0.0078 s and the displacement of the bearing is equal to -2.495e-4 mm and after 0.0108 s for the second time the rotor contacts the bearing and the displacement of the bearing is equal to -1.650e-4 mm.



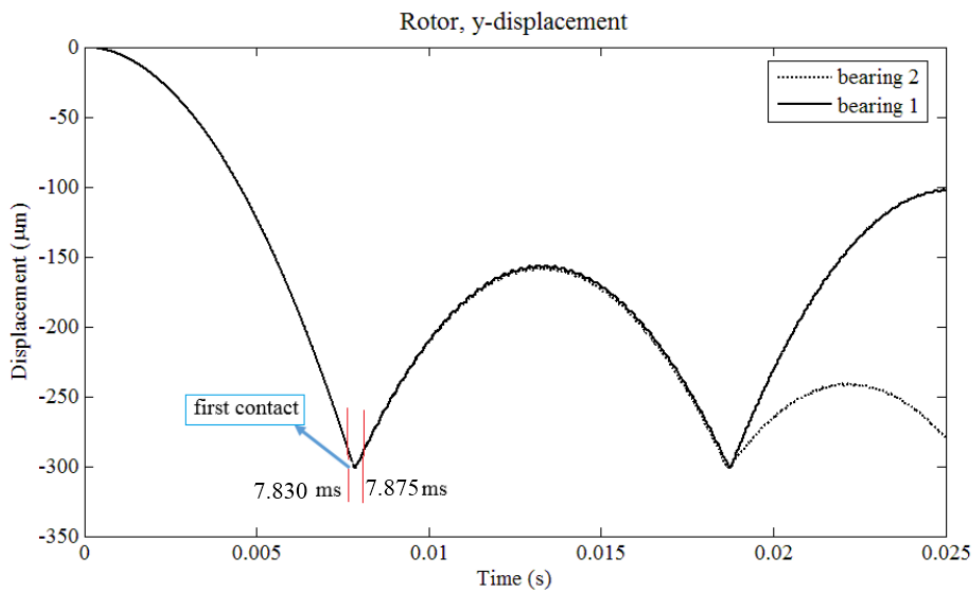**Figure 3.3.** Rotor displacement in $y$-direction, dropdown time at zero rpm, clearance 1 μm.
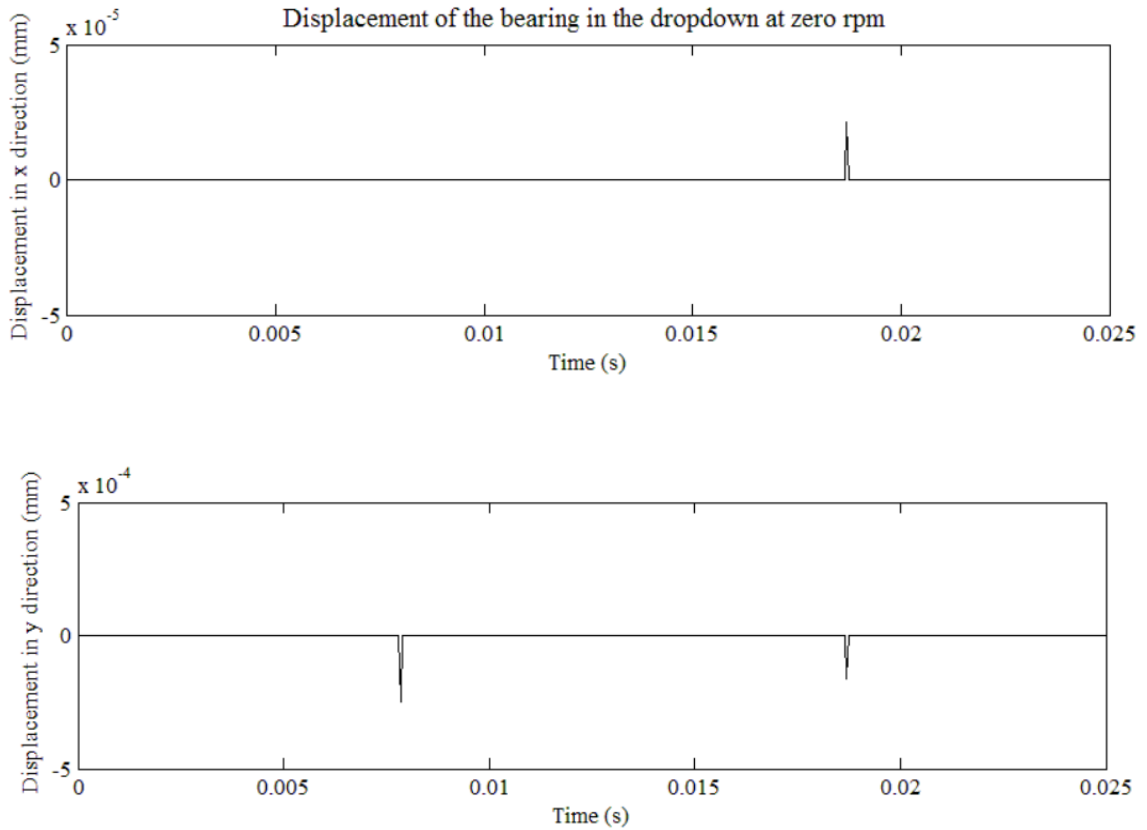
**Figure 3.4.** Displacement of the bearing in whole simulation of the dropdown at zero rpm.

Figure 3.5 and 3.6 show the displacement of the bearing in $x$ and $y$-direction during the first contact, respectively. The contact occurs from 7.830 to 7.875 ms. The displacement of the bearing along $z$-direction ($e_z$) is assumed to be zero. Therefore, the vector of the displacement ($e_x, e_y, e_z$) can be obtained. These displacements were used to obtain the penetration of the ball in the inner race (equation (2.74)). In this work the ball number starts from one at zero degree in counter clockwise (Figure 3.7).
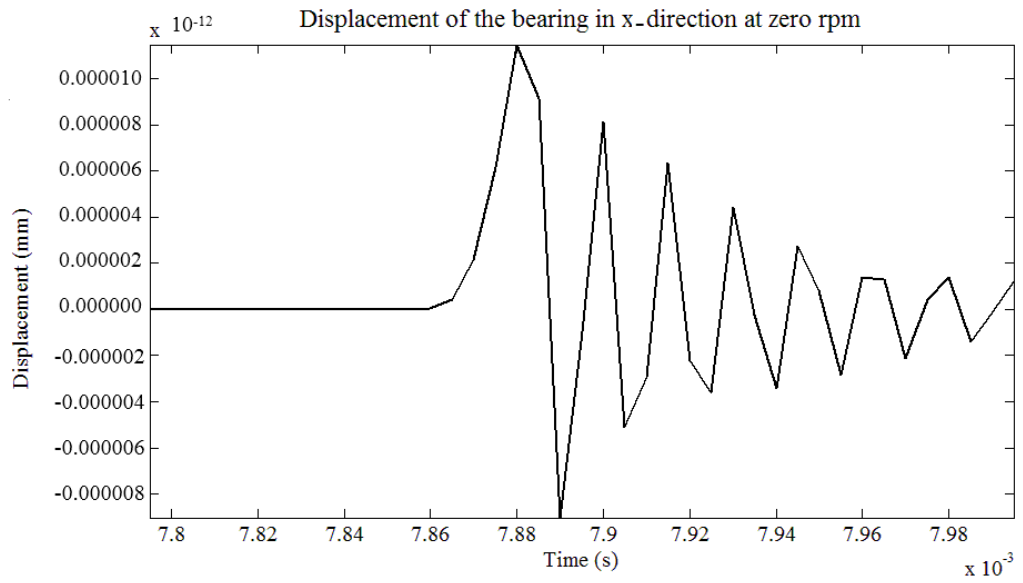
**Figure 3.5.** Bearing displacement in $x$-direction during the first contact, dropdown at zero rpm, clearance 1 μm.
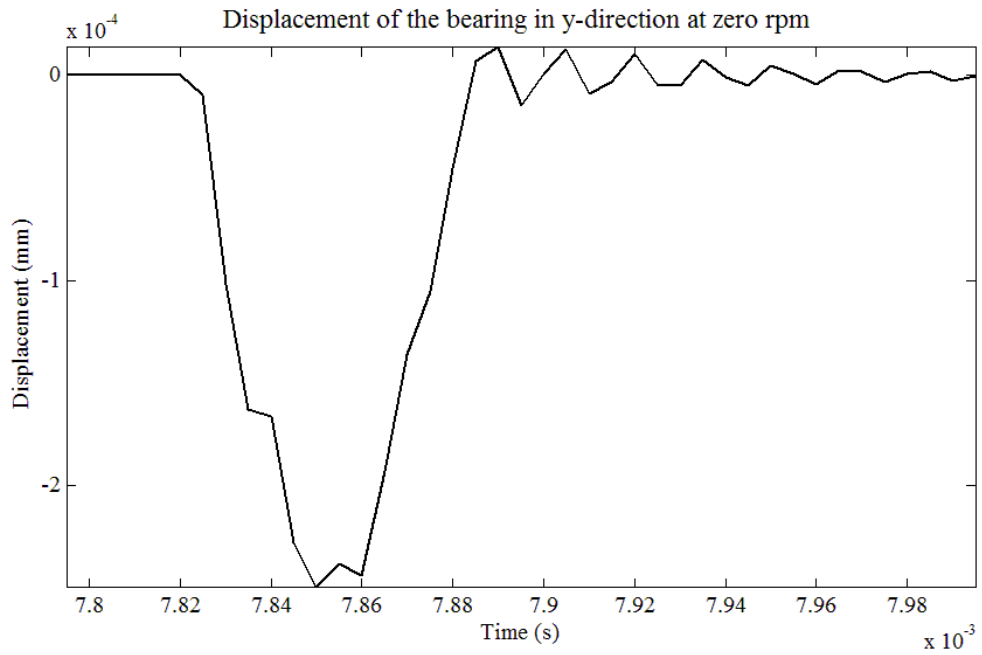


**Figure 3.6.** Bearing displacement in $y$-direction during the first contact, dropdown at zero rpm, clearance 1 μm.
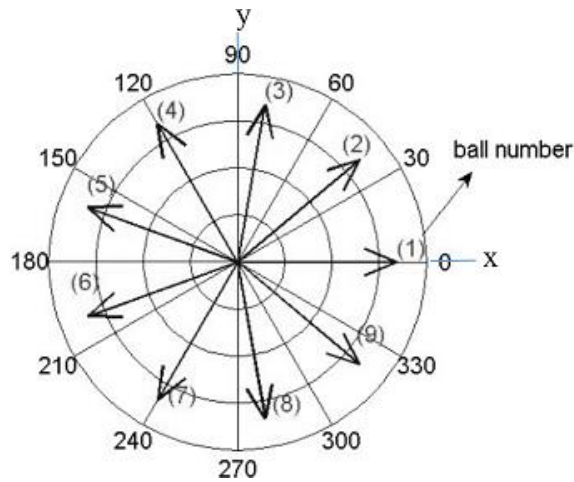
**Figure 3.7.** Position of the balls in the bearing.

In order to obtain the maximum Hertzian contact stresses, the locations were the balls contact inner race and the deformations have the positive magnitude should be taken into account. These locations determine the positions were the balls penetrate into the inner race. The simulation reveals that from 7.830 to 7.875 ms the limited number of balls penetrate into inner race. In the rest of the simulation time balls do not penetrate into the inner race and the stress is equal to zero.

The data in Table 3.3 shows that at this time step, the deformation of the ball number 7, 8 and 9 have a positive value and the balls penetrate into inner race. In addition to these balls, the ball number 6 also contacts the inner race. However, the contact time of the ball 6 is shorter that other three balls (7.835 to 7.865 ms). Figure 3.8 reveals the information about the normal contact forces between the ball 6, 7, 8, 9 and inner race. It has been found that from 7.830 to 7.850 ms, the normal force on the ball number 6, 7, 8, 9 has a gradual increase until 7.850 ms. For the next 0.025 ms the normal force dropped to approximately it's value at 7.830 ms. The maximum normal contact force is equal to 22.91 N (ball 8). The normal force of ball 6, 7, 9 has a considerable difference with normal force of ball 8 (1.76, 17.91 N and 9.71 N, respectively).

*Table 3.3. Deformation of the inner race (m), dropdown at zero rpm, clearance 1 μm.*

| Ball number | Time (ms) | | | | | | | | | |
|---|---|---|---|---|---|---|---|---|---|---|
| | **7.830** | **7.835** | **7.840** | **7.845** | **7.850** | **7.855** | **7.860** | **7.865** | **7.870** | **7.875** |
| 1 | -5e-07 | -5e-07 | -5e-07 | -5e-07 | -5e-07 | -5e-07 | -5e-07 | -5e-07 | -5e-07 | -5e-07 |
| 2 | -1.15e-06 | -1.54e-06 | -1.56e-06 | -1.96e-06 | -2.10e-06 | -2.02e-06 | -2.06e-06 | -1.74e-06 | -1.37e-06 | -1.17e-06 |
| 3 | -1.50e-06 | -2.10e-06 | -2.13e-06 | -2.74e-06 | -2.95e-06 | -2.84e-06 | -2.89e-06 | -2.40e-06 | -1.84e-06 | -1.53e-06 |
| 4 | -1.38e-06 | -1.90e-06 | -1.94e-06 | -2.47e-06 | -2.66e-06 | -2.55e-06 | -2.60e-06 | -2.17e-06 | -1.67e-06 | -1.41e-06 |
| 5 | -8.47e-07 | -1.05e-06 | -1.06e-06 | -1.27e-06 | -1.35e-06 | -1.31e-06 | -1.33e-06 | -1.16e-06 | -9.65e-07 | -8.59e-07 |
| 6 | -1.52e-07 | 5.62e-08 | 6.88e-08 | 2.78e-07 | 3.53e-07 | 3.13e-07 | 3.33e-07 | 1.60e-07 | -3.44e-08 | -1.40e-07 |
| 7 | 3.80e-07 | 9.08e-07 | 9.40e-07 | 1.47e-06 | 1.66e-06 | 1.55e-06 | 1.60e-06 | 1.17e-06 | 6.78e-07 | 4.10e-07 |
| 8 | 5.01e-07 | 1.10e-06 | 1.13e-06 | 1.74e-06 | 1.95e-06 | 1.84e-06 | 1.89e-06 | 1.40e-06 | 8.40e-07 | 5.35e-07 |
| 9 | 1.53e-07 | 5.45e-07 | 5.69e-07 | 9.63e-07 | 1.10e-06 | 1.02e-06 | 1.06e-06 | 7.40e-07 | 3.75e-07 | 1.75e-07 |
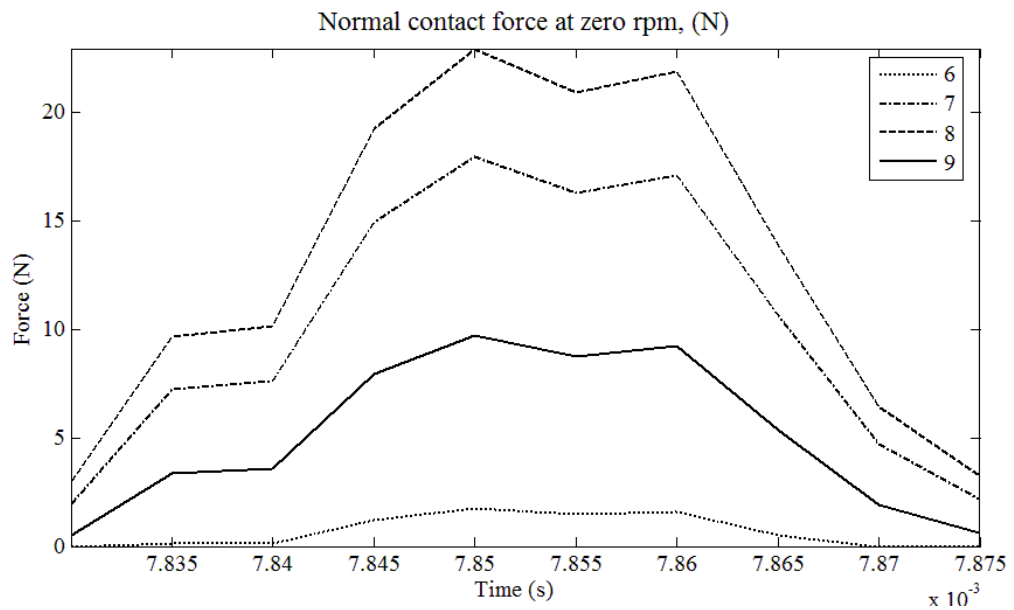


**Figure 3.8.** Normal force in dropdown at zero rpm, clearance 1 μm.

The maximum Hertzian stress of ball 6, 7, 8, 9 is depicted in Table 3.4. The data in Table 3.4 shows the maximum stress occurs at 7.850 ms. The stress distribution at 7.850 ms is depicted in Figure 3.9. At 7.850 ms, the ball 8 has the maximum stress is equal to 1336 MPa.

*Table 3.4. The Maximum Hertzian contact stress and as a result of penetration of the ball on inner race (MPa), dropdown at zero rpm, clearance 1 μm.*

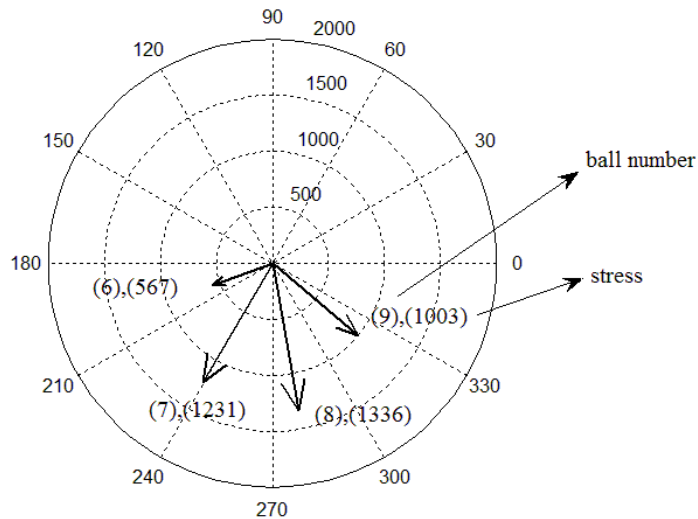| Clearance (μm) | Ball number | Time (ms) | | | | | | | | | |
|---|---|---|---|---|---|---|---|---|---|---|---|
| | | 7.830 | 7.835 | 7.840 | 7.845 | 7.850 | 7.855 | 7.860 | 7.865 | 7.870 | 7.875 |
| 1 | 6 | - | 226 | 250 | 504 | 567 | 534 | 551 | 382 | - | - |
| | 7 | 589 | 910 | 926 | 1158 | 1231 | 1193 | 1211 | 1034 | 787 | 612 |
| | 8 | 676 | 1002 | 1019 | 1260 | 1336 | 1296 | 1316 | 1130 | 875 | 699 |
| | 9 | 374 | 705 | 720 | 937 | 1003 | 968 | 986 | 822 | 585 | 400 |



**Figure 3.9.** Maximum Hertzian stress at 7.850 ms, dropdown at zero rpm, clearance 1 μm.

Figure 3.10 shows the stresses in the ball 6, 7, 8 and 9 between 7.830 to 7.875 ms. It has been found that at 7.830 ms (when the rotor starts to descend) the ball starts to penetrate into the inner race, the stresses for the ball number 7, 8 and 9 are equal to 589, 676 and 374 MPa, respectively. At 7.830 ms the ball 6 does not contact to inner race. The data obtained from the stress analysis shows that by increasing the displacement of the rotor the maximum contact stress will gradually rise. The result are consistent with the maximum displacement of the rotor. At 7.850 ms the displacement of the rotor in $y$-direction reaches to its maximum

value (-2.5e-4 mm), the stresses on the ball surge to 1336 MPa. From 7.850 to approximately 7.875 ms the magnitude of the displacement will decrease. Therefore, the stress value will decline and finally at 7.875 ms the stress is just slightly higher than the stress at 7.830 and the stresses for ball 7, 8 and 9 are equal to 612, 699 and 400 MPa, correspondingly.
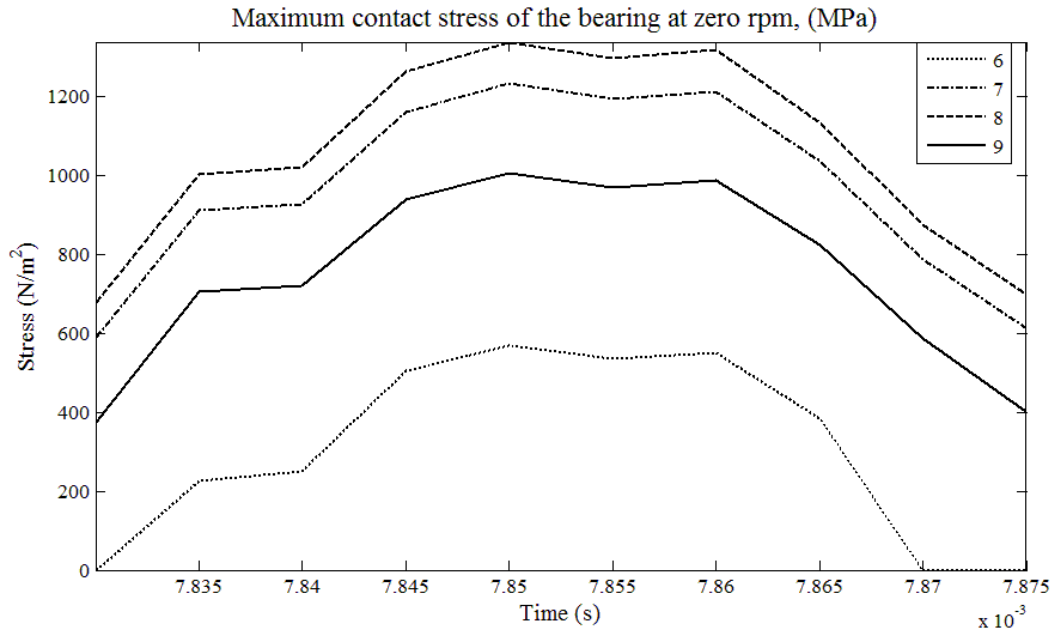


**Figure 3.10.** Maximum Hertzian stress, dropdown at zero rpm, clearance 1 μm.

3.3 Stress in the dropdown of the rotor at 9000 rpm and the bearing clearance 1 μm

Second case investigates the stresses in the dropdown at 9000 rpm and the nominal bearing clearance equal to 1 μm. The displacement of the rotor in $x$ and $y$-direction are shown in Figure 3.11 and 3.12, respectively. Figure 3.13 and 3.14 depict the displacements of the bearing (during the first contact) in $x$ and $y$-direction, correspondingly. The displacement of the bearing in $y$-direction is similar to the displacements of the bearing in the dropdown at zero rpm. In previous case the displacement of the bearing in in $x$-direction was practically zero while in the second case it has higher value (3.8e-5 mm). At 7.850 ms, the displacement of the bearing in both $x$ and $y$-direction reaches to the maximum value (3.8e-5 mm, -2.5e-4 mm).
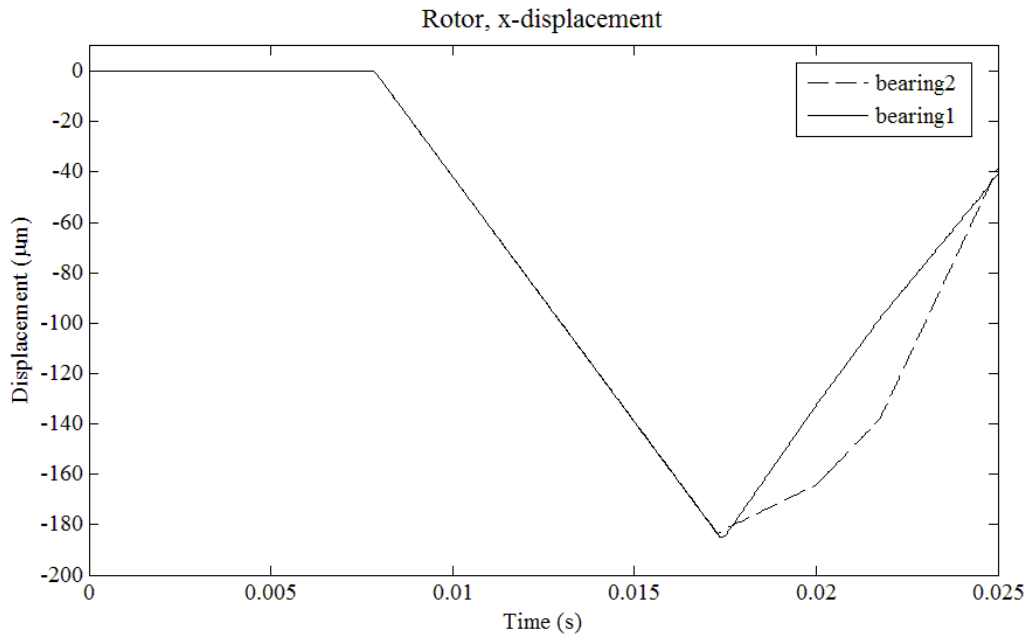
**Figure 3.11.** Rotor displacement in $x$-direction during the dropdown time at 9000 rpm, clearance 1 μm.
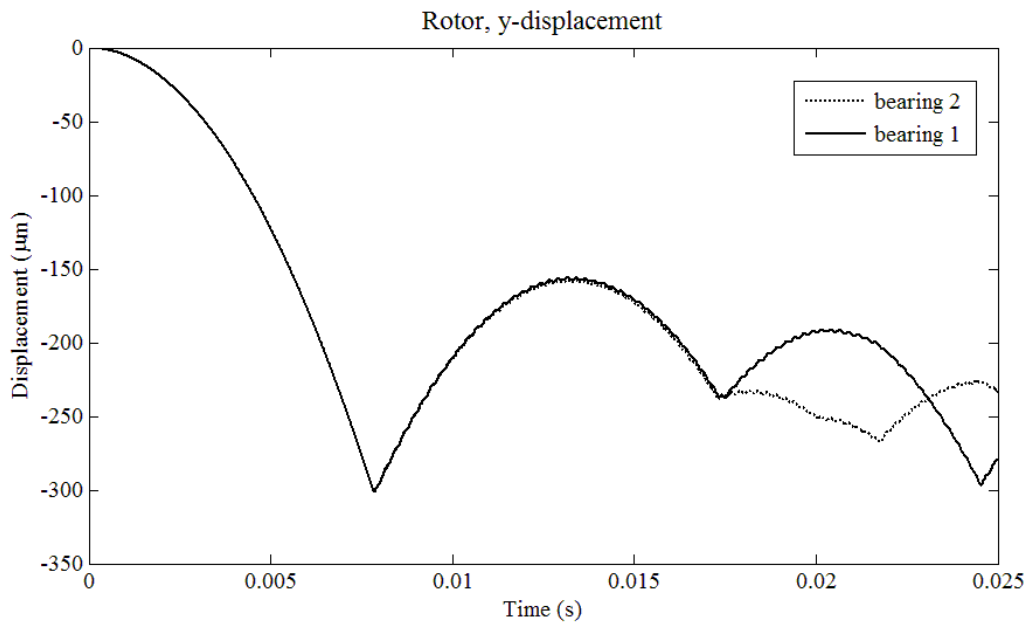


**Figure 3.12.** Rotor displacement in $y$-direction, dropdown time at 9000 rpm, clearance 1 μm.
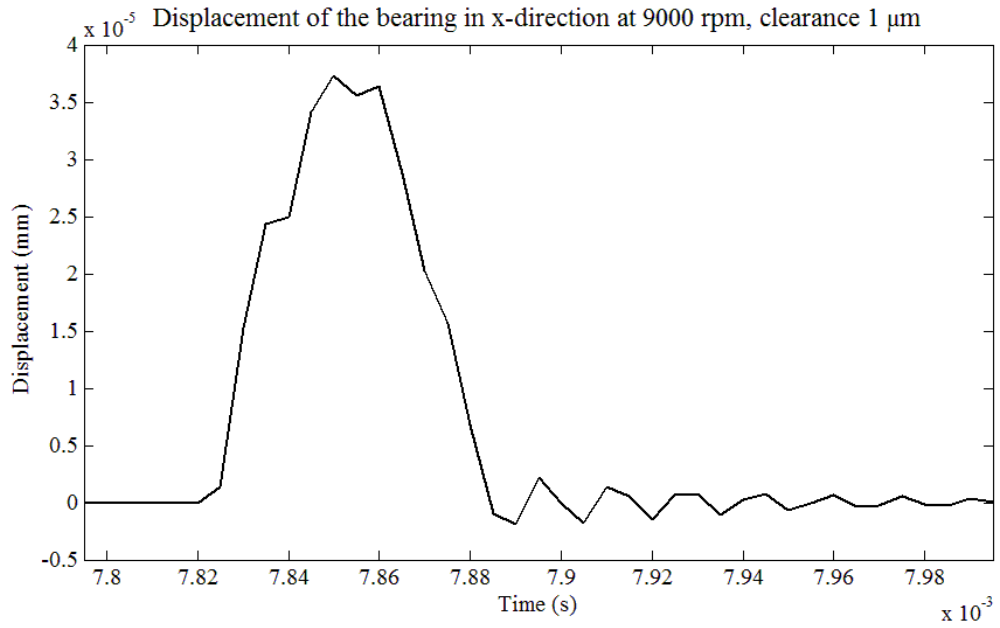
**Figure 3.13.** Bearing displacement in $x$-direction during the first contact, dropdown at 9000 rpm, clearance 1 μm.
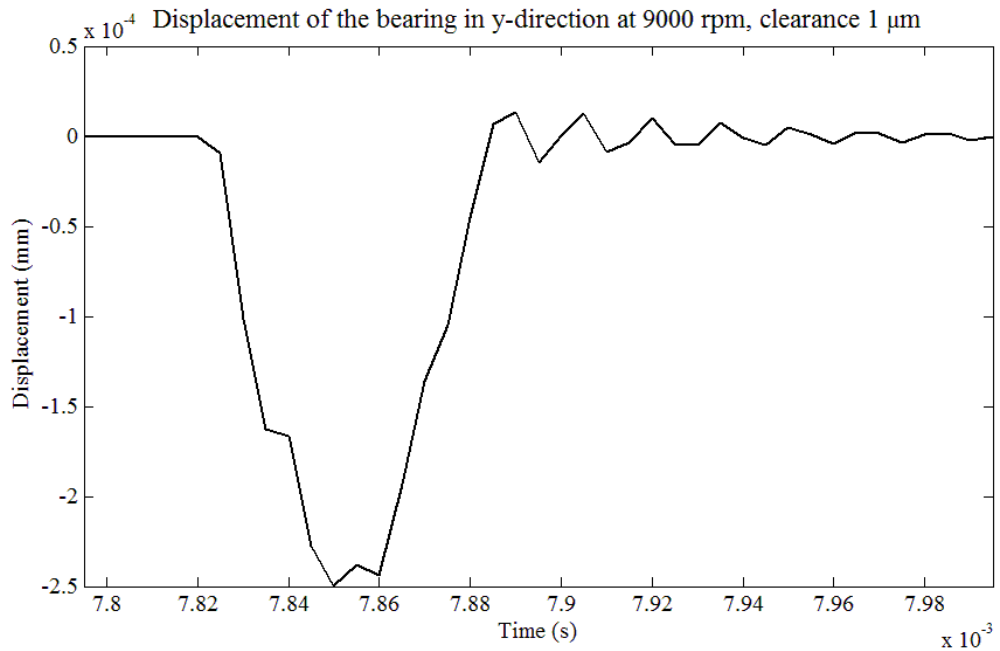


**Figure 3.14.** Bearing displacement in $y$-direction during the first contact, dropdown at 9000 rpm, clearance 1 μm.

The data in Table 3.5 shows that from 7.830 to 7.875 ms, the deformation of the ball number 7, 8 and 9 have a positive value. The ball 6 contacts inner race only at 7.850 ms and the deformation of bearing is very low. Therefore, in the calculation of force and stress this ball is neglected. Figure 3.15 reveals the normal force between the balls and inner race has a similar pattern to the normal force in the dropdown at zero rpm. However, the force magnitude is higher than the normal force in the dropdown at zero rpm. The highest normal force is equal to 24 N between ball 8 and inner race.

*Table 3.5. Deformation of the inner race (m), dropdown at 9000 rpm, clearance 1 μm.*

| Ball number | Time (ms) | | | | | | | | | |
|---|---|---|---|---|---|---|---|---|---|---|
| | 7.830 | 7.835 | 7.840 | 7.845 | 7.850 | 7.855 | 7.860 | 7.865 | 7.870 | 7.875 |
| 1 | -3.85e-07 | -2.56e-07 | -2.51e-07 | -1.59e-07 | -1.27e-07 | -1.45e-07 | -1.36e-07 | -2.12e-07 | -2.97e-07 | -3.43e-07 |
| 2 | -1.04e-06 | -1.36e-06 | -1.38e-06 | -1.70e-06 | -1.82e-06 | -1.76e-06 | -1.79e-06 | -1.52e-06 | -1.22e-06 | -1.06e-06 |
| 3 | -1.47e-06 | -2.06e-06 | -2.09e-06 | -2.68e-06 | -2.89e-06 | -2.78e-06 | -2.84e-06 | -2.35e-06 | -1.81e-06 | -1.51e-06 |
| 4 | -1.46e-06 | -2.03e-06 | -2.06e-06 | -2.64e-06 | -2.85e-06 | -2.74e-06 | -2.79e-06 | -2.32e-06 | -1.78e-06 | -1.49e-06 |
| 5 | -9.91e-07 | -1.29e-06 | -1.30e-06 | -1.60e-06 | -1.70e-06 | -1.65e-06 | -1.67e-06 | -1.43e-06 | -1.16e-06 | -1.01e-06 |
| 6 | -2.96e-07 | -1.73e-07 | -1.65e-07 | -4.17e-08 | 2.62e-09 | -2.06e-08 | -8.72e-09 | -1.10e-07 | -2.25e-07 | -2.87e-07 |
| 7 | 3.04e-07 | 7.87e-07 | 8.16e-07 | 1.30e-06 | 1.47e-06 | 1.38e-06 | 1.43e-06 | 1.03e-06 | 5.78e-07 | 3.33e-07 |
| 8 | 5.28e-07 | 1.14e-06 | 1.18e-06 | 1.80e-06 | 2.02e-06 | 1.90e-06 | 1.96e-06 | 1.45e-06 | 8.76e-07 | 5.63e-07 |
| 9 | 2.70e-07 | 7.32e-07 | 7.60e-07 | 1.22e-06 | 1.39e-06 | 1.30e-06 | 1.34e-06 | 9.61e-07 | 5.30e-07 | 2.96e-07 |
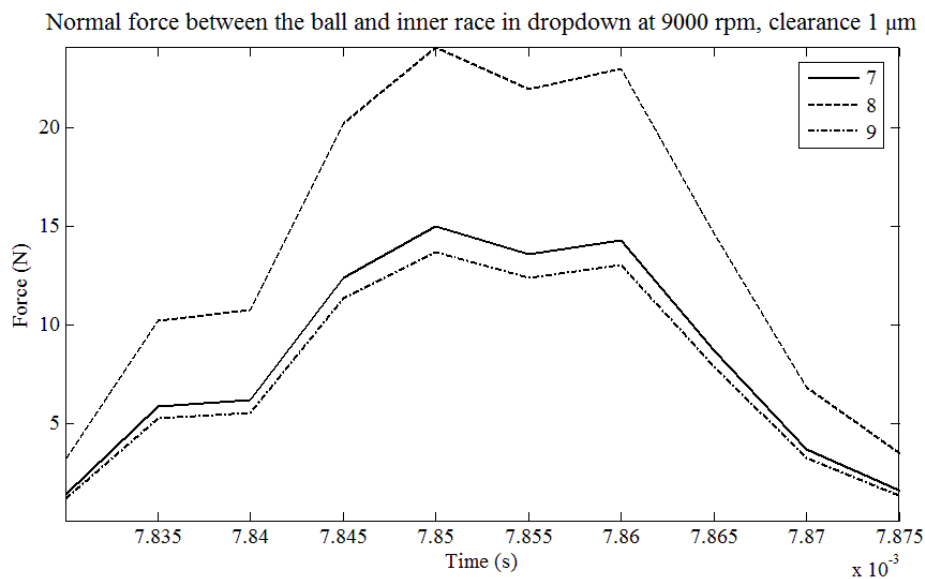


**Figure 3.15.** Normal force in dropdown at 9000 rpm, clearance 1 μm.

Table 3.6 shows the maximum stress occurs at 7.850 ms and the stress distribution at this moment is depicted in Figure 3.16. The same as previous case, the ball number 8 has the highest stress (1359 MPa).

*Table 3.6. Maximum Hertzian contact stress as a result of penetration of the ball on inner race (MPa), dropdown at 9000 rpm, clearance 1 μm.*

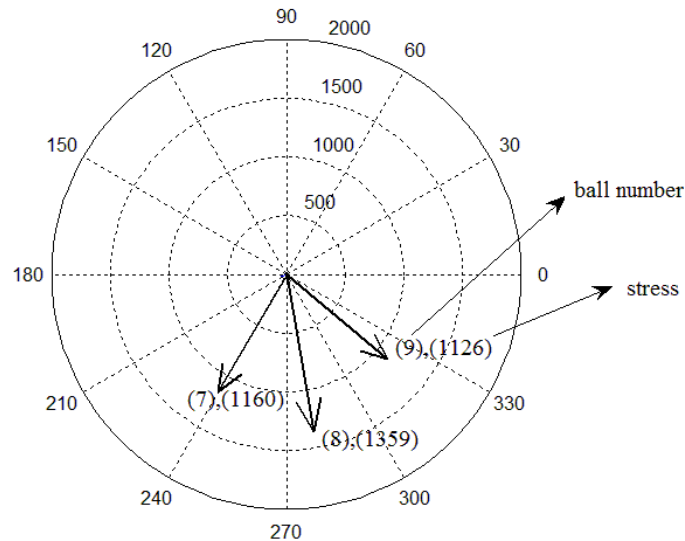| Clearance (μm) | Ball number | Time (ms) | | | | | | | | | |
|---|---|---|---|---|---|---|---|---|---|---|---|
| | | 7.830 | 7.835 | 7.840 | 7.845 | 7.850 | 7.855 | 7.860 | 7.865 | 7.870 | 7.875 |
| 1 | 7 | 526 | 847 | 862 | 1089 | 1159 | 1123 | 1141 | 968 | 726 | 550 |
| | 8 | 693 | 1021 | 1038 | 1282 | 1359 | 1318 | 1338 | 1150 | 894 | 716 |
| | 9 | 496 | 817 | 832 | 1057 | 1126 | 1089 | 1107 | 936 | 695 | 519 |



**Figure 3.16.** Maximum Hertzian stress at 7.850 ms, dropdown at 9000 rpm, clearance 1 μm.

At 7.830 ms the stresses for the ball number 7, 8 and 9 are equal to 526, 693 and 496 MPa, respectively. The result of stress analysis also have the same pattern as previous case (see Figure 3.17). As the displacement of the bearing increases the stresses become greater and

at 7.850 ms it has the maximum value equal to 1359 MPa (ball 8). Then, from 7.850 to 7.875 ms the magnitude of the displacement declined and the stress value for ball 7, 8, 9 dropped to 550, 716 and 519 MPa. In this case only three balls are in contact with inner race and the overall value of stresses are higher than dropdown at zero rpm.
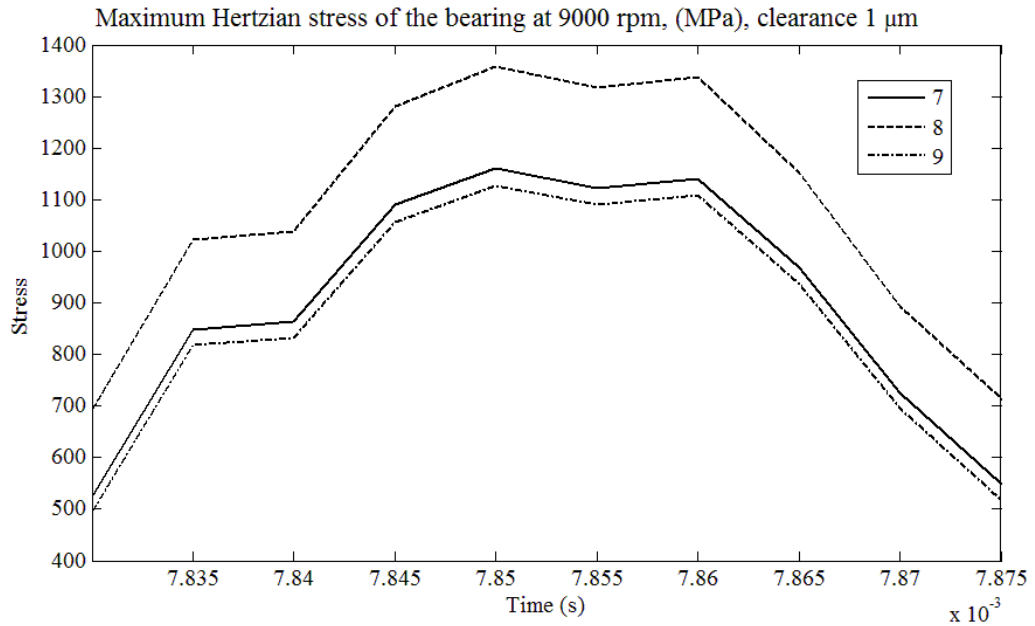


**Figure 3.17.** Maximum Hertzian stress, dropdown at 9000 rpm, clearance 1 μm.

3.4 Stress in the dropdown of the rotor at 9000 rpm and the bearing clearance 5 μm

This part features the results of simulation in the dropdown at 9000 rpm and the bearing clearance is increased to 5 μm. The complete investigation of the effect of bearing clearance requires the new simulation of the rotor dropdown and extracting the corresponding data. Figure 3.18 and 3.19 depict the displacements of the bearing in $x$, $y$-direction in the dropdown at 9000 rpm and the nominal bearing clearance is equal to 5 μm. These displacements are similar to the displacements of the bearing in the second case.
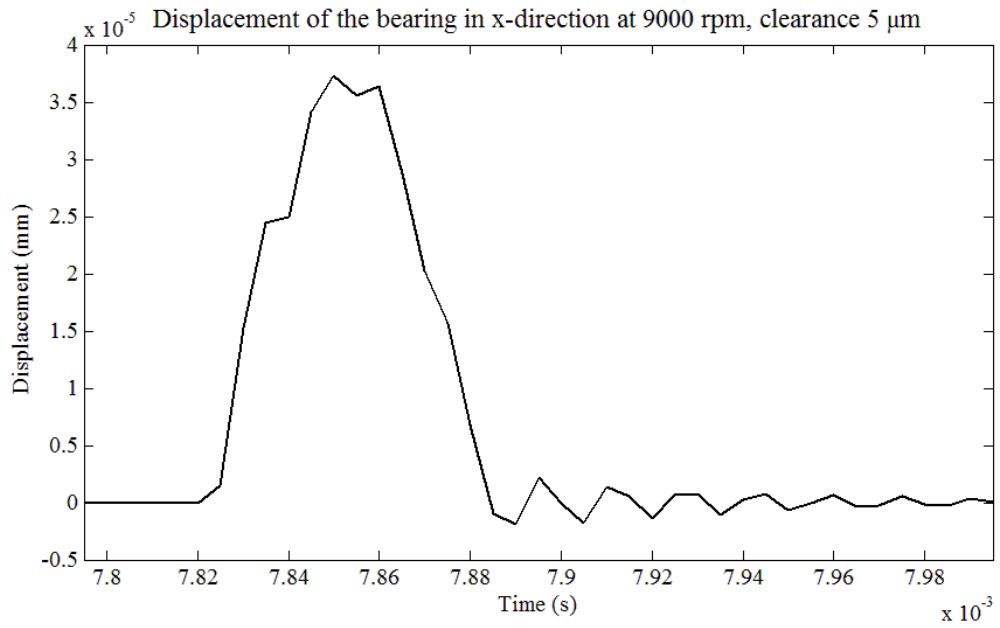
**Figure 3.18.** Bearing displacement in $x$-direction during the first contact, dropdown at 9000 rpm, clearance 1 μm.
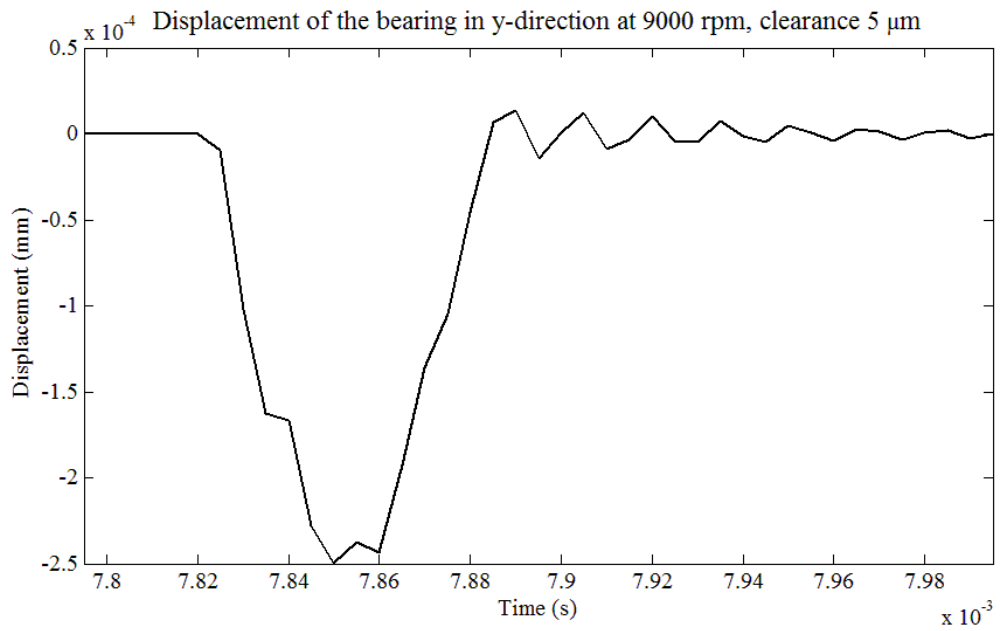


**Figure 3.19.** Bearing displacement in $y$-direction during the first contact, dropdown at 9000 rpm, clearance 5 μm.

As can be seen in Figure 3.20 and 3.21 the displacements of the bearing with 1 and 5 µm clearance have an infinitesimal difference. Therefore, it is expected that the stresses will not have a considerable differences.
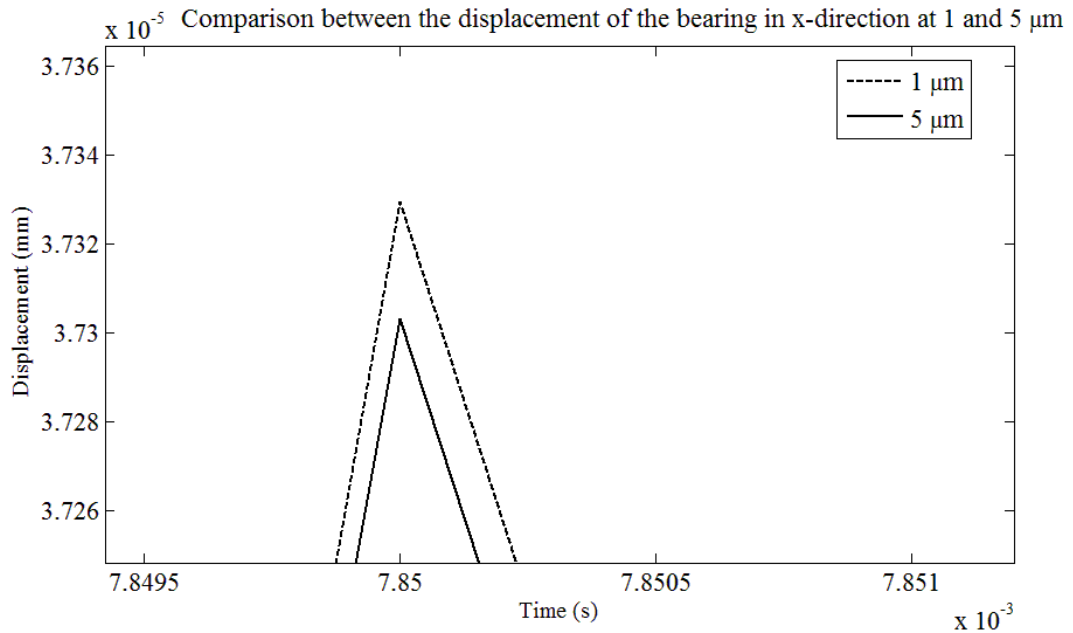


**Figure 3.20.** Comparison between the displacement of the bearing in $x$-direction at 1 and 5 µm clearance.
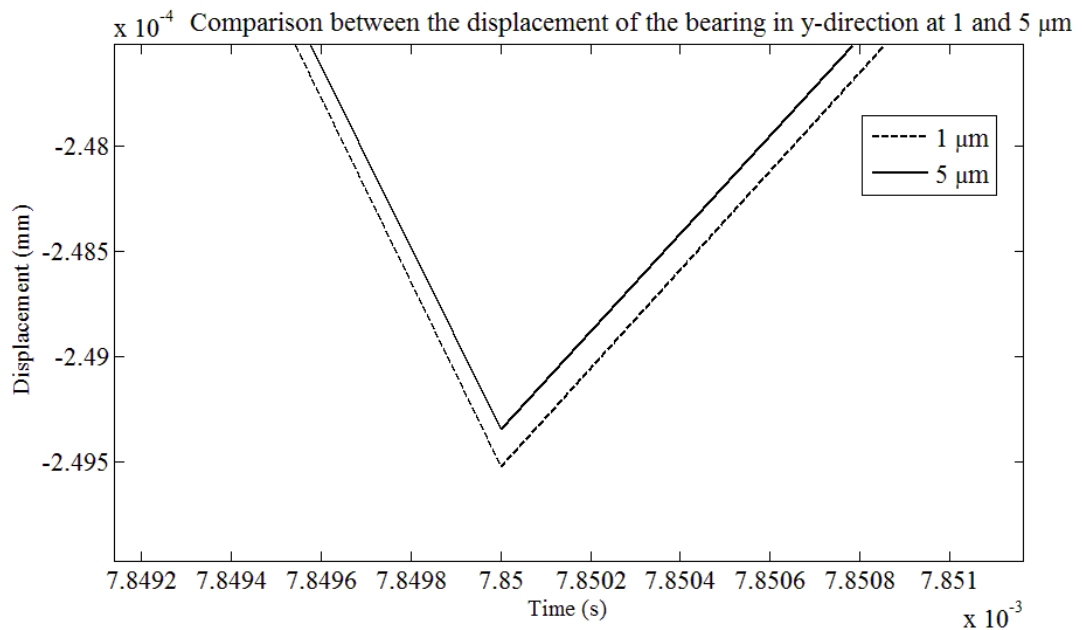


**Figure 3.21.** Comparison between the displacement of the bearing in $x$-direction at 1 and 5 µm clearance.

The same as previous cases, only from 7.830 to 7.875 ms the inner race deforms as a result of the contact with ball 7, 8 and 9. Table 3.7 also shows that at 7.850 ms, the maximum Hertzian stress is equal to 1357 MPa (in second case it was 1359 MPa). The Hertzian contact stresses of these balls is depicted in Figure 3.22. The overall pattern of the stress is compatible with the displacement in the bearing. By increasing the displacement of the bearing the stress magnitude is raised and vice versa. It should be noted that the displacement of the bearing in $y$-direction is higher than the displacement in $x$-direction. Therefore, the stresses are more influenced by the vertical displacement.

*Table 3.7. Maximum Hertzian contact stress as a result of penetration of the ball on inner race (MPa), dropdown at 9000 rpm, clearance 5 μm.*

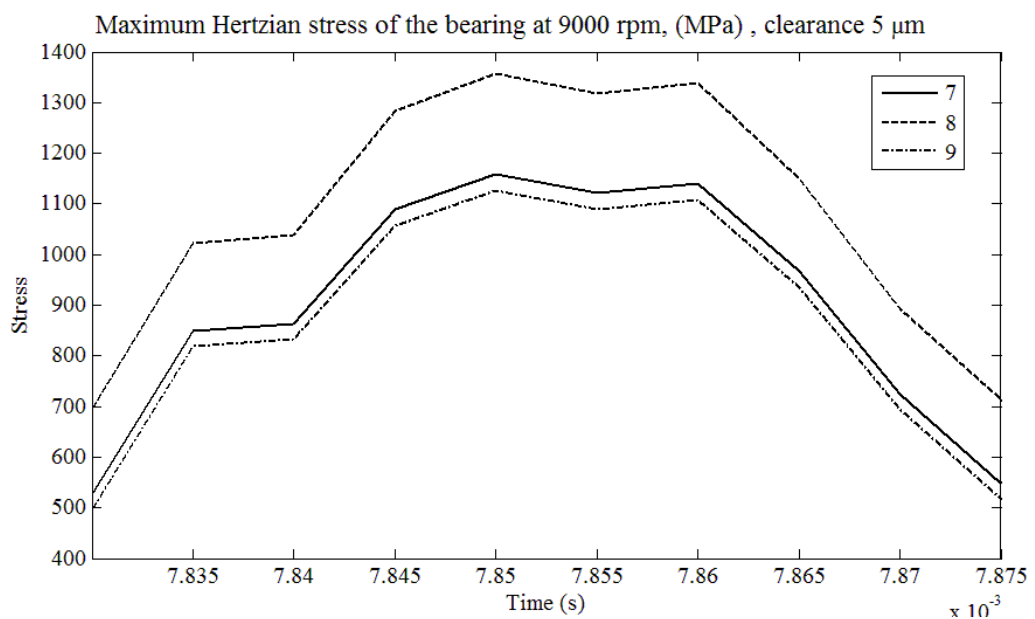| Clearance (μm) | Ball number | Time (ms) | | | | | | | | | |
|---|---|---|---|---|---|---|---|---|---|---|---|
| | | 7.830 | 7.835 | 7.840 | 7.845 | 7.850 | 7.855 | 7.860 | 7.865 | 7.870 | 7.875 |
| 1 | 7 | 528 | 848 | 863 | 1090 | 1159 | 1122 | 1141 | 967 | 725 | 550 |
| | 8 | 695 | 1022 | 1038 | 1282 | 1357 | 1317 | 1337 | 1149 | 893 | 716 |
| | 9 | 498 | 818 | 833 | 1057 | 1125 | 1089 | 1107 | 935 | 695 | 519 |



**Figure 3.22.** Maximum Hertzian stress, dropdown at 9000 rpm, clearance 5 μm.

# 4   DISCUSSION

In this study, the Hertzian stress has been applied to calculate the stresses for the touchdown bearing with three conditions. The simulation reveals that in the dropdown the normal load between the ball and inner race does not have a uniform effect on all balls. Investigation of the deformation of the bearing in Table 3.3 and Table 3.5 shows in the first contact dependent on the dropdown condition different number of balls can penetrate into inner race. Previous studies also imply that dependent on the magnitude and direction of the impact force and also position of the ball, the limited number of the balls can carry the load [27, pp. 54-61]. Generally, lower than half of the total number of the balls carry the load. This area also referred as load zone. The number of the balls carrying the load (N) can be calculated by [28, p. 2]:

$$N = INT \left( \frac{n - 1}{4} \right) \tag{4.1}$$

where $INT$ is integer. In this simulation the $n=9$ ($n$ is total number of ball), therefore above equation shows that at certain time 2 out of 9 balls are under load. The outcome of simulation of the stresses in the dropdown at 9000 rpm shows that in the dropdown ball number 7, 8 and 9 had a positive deformation. In the dropdown at zero rpm ball 6 is also in contact with inner. These balls located in the lower half of the bearing and they carry the load. In addition, the negative deformation on upper half of the bearing has a good agreement with [28, p. 5] that demonstrated the gap between the ball and inner race in upper half of the bearing. It should be considered that in the dropdown at zero rpm the higher number of balls rather than dropdown at 9000 rpm are in contact with inner race and the stress level in the dropdown at zero rpm is less than 9000 rpm. However, the number of balls that are in contact with inner race is not the only parameter that can influence on the stress level.

Figure 3. 5 shows that when the dropdown occurs at zero rpm the displacement of the bearing in $x$-direction is practically zero (10e-18 mm). At zero rpm the rotor hits the bearing down

and after impact bounces back. The displacement of the bearing in $y$-direction is less than the displacement in 9000 rpm. In this case the maximum Hertzian stress is 1336 MPa (Figure 3.10).

In addition, Figure 3.13-14 showed that in the dropdown at 9000 rpm and the nominal bearing clearance equal to 1 μm, the displacement of the bearing in $y$-direction is approximately ten times higher than the displacement of the bearing in $x$-direction. Therefore, the results are mainly affected by the displacement of the bearing in vertical direction. Figure 3.15 reveals that the increase or reduction in the normal force between the ball and inner race depends on the displacement of the bearing. When the displacement increases (mainly in $y$-direction) the normal force is raised and at 7.850 reaches to highest magnitude of 24 N (ball 8), then by decreasing the displacement of the bearing from 7.850 to 7.875 ms the normal force is reduced. It should be noted that the normal load between ball 7 and inner race is slightly higher that the corresponding load for ball 9. This difference can be attributed to the initial assumption in position of ball 1 at 0 degree (Figure 3.7). In this study the number of ball was odd and it is expected that for even number of ball the normal load between ball and inner race will be symmetric with respect to the bearing $y$-axis. The similar behavior has been observed in Figure 3.17 for the maximum Hertzian stress at dropdown in 9000 rpm and 1 μm clearance. Furthermore, it should be considered that the relation between the normal contact force and the deformation of the inner race is not linear (equation (2.65)), this causes the analysis of the contact of ball on inner race became complicated. The deformation of the inner race in the rotor dropdown depends on the geometric and material properties of the bearing and the forces exerted to the bearing.

In addition, the maximum Herzian stress depends on the normal force and the semi-minor and major axes of the elliptic area (equation (2.77)). But the semi-minor and major axes are also affected by the normal force and the contact stiffness (equation (2.59)). The displacement of the bearing for the third case with higher clearance (dropdown at 9000 rpm and 5 μm clearance) were shown in Figure 3.18 and 3.19. These displacements are close to

displacement of the bearing during dropdown at 9000 rpm and 5 μm clearance. In this case the maximum Herzian stress is only 2 MPa lower than first case (At 7.850 ms, the ball 8 has the maximum Herzian stress equal to 1357 MPa (Figure 3.22)). The overall stress distribution is similar to previous cases. Hence, the maximum Hertzian stress depends not only on the location of the ball, but also on the geometrical and material property of bearing and the behavior of the rotor in the dropdown. As in AMB system the rotor might experience several dropdowns, it is important to compare the calculated stress value with the maximum allowable contact stress.

Göncz et al. [29, pp. 174-184] studied the maximum allowable contact loading on the races. Their work indicates that for the conventional steel bearing 100Cr6 (Chrome steel balls), the maximum contact stress for ball bearing is equal to 4200 MPa and for the roller bearing it is equal to 4000 MPa. The hardness and material property of the bearing can affect the acceptable limit for contact stress in ball bearing. Wang and Yuan [30, p. 229-236] suggested that for the steel bearing 42CrMo (Chrome Molybdenum) and hardness of 55 HRC (Rockwell C-Scale Hardness) the maximum allowable contact stress for point contact is 3850 MPa and for line contact 2700 MPa. For the ring with 50 Mn (Manganese), the maximum allowable stress for point contact proposed to be 3400 MPa and for line contact is equal to 2200 MPa. In current study, the maximum contact stress is equal to 1359 MPa that is less that maximum allowable contact stress. In improper operating condition of the machinery, the fatigue failure of the bearing might initiate even in less than the maximum allowable contact stress. Therefore, a lower limit for maximum contact stress can be considered.

# 5   CONCLUSION AND FURTHER STUDIES

In this study the Hertzian contact model was applied to obtain the stresses in the touchdown bearing of the AMB supported rotor during dropdown event. The Hertzian stress model is an analytical method for obtaining the contact stress. By applying this method, instead of the point contact between the ball and bearing race, the elliptic area was calculated to obtain the stress. The literature review showed that the elliptical parameters can be obtained from several approximations. Previous studies described that the error of applying the Hertzian contact stress is less than 3% of the experimental results.

Present research focused to obtain the stresses in the first contact of the rotor with touchdown bearing. In this work, the normal force and the maximum contact stress between each ball and inner race were calculated. The contact stress on the bearing depends on the geometry and material property of the bearing and also the behavior of the rotor in the dropdown. The calculation of the stresses in touchdown bearing requires to apply an appropriate model for simulation of the dropdown and the bearing model.

This study showed that in the dropdown the radial force is not equally distributed in the touchdown bearing and few number of the balls located in the lower half of the bearing carrying the load. In the dropdown at zero rpm 4 out of 9 and in dropdown at 9000 rpm 3 out of 9 balls were under load. It should be noted that in the dropdown the rotor will contact the bearing in several points and above result is valid for the first contact and it is expected that in the next contacts the position of the maximum Hertzian stress will be changed.

In addition, the simulation revealed that the maximum Hertzian contact stress is highly affected by the displacement of the bearing in vertical direction. By increasing the displacement of the bearing the maximum Hertzian stress raised and vice versa. It should be considered that the relation between the normal force and maximum Hertzian stress with the

deformation of the inner race is not linear. Furthermore, the speed of the rotor in the dropdown influences the maximum stress in touchdown bearing. The investigation of three conditions for the case study showed that when the dropdown occurs at higher speed, the stress level is increased.

In future, by applying the more developed model for bearing, the effect of centrifugal force, gyroscopic effect can be included in model and the stress between the ball and both races can be calculated. Moreover, the friction force between the ball and inner race creates a heat source. Therefore, the thermal model of the bearing components can be developed. Then, by making electric circuits equivalent model of heat transfer, the temperature rise in the bearing can be calculated. Thus, the effect of the thermal expansion will be considered in calculation of the deformation of bearing race. Finally, the rainflow analysis can be done to obtain the stress history of the touchdown bearing and it gives more accurate result in estimating the life of the bearing.

# REFERENCES

[1] Kärkkäinen, A., Sopanen, J. & Mikkola, A. Dynamic simulation of a flexible rotor during drop on retainer bearings. Journal of Sound and Vibration, 2007. Vol. 306:3-5. pp. 601-617.

[2] Halminen, O., Kärkkäinen, A., Sopanen, J. & Mikkola, A. Active magnetic bearing-supported rotor with misaligned cageless backup bearings: A dropdown event simulation model. Mechanical Systems and Signal Processing, 2015. Vol. 50-51. pp. 692-705.

[3] Cole, M. O. T., Keogh, P. S. & Burrows, C. R. The dynamic behavior of a rolling element auxiliary bearing following rotor impact. ASME Journal of Tribology, 2002. Vol. 124:2. pp. 406-413.

[4] Schweitzer, G. & Maslen, E. H. (editors) Magnetic Bearings Theory: Design, and Application to Rotating Machinery. Springer -Verlag Berlin Heidelberg, 2009. 535 p.

[5] Kurvinen, E., Sopanen, J. & Mikkola, A. Ball bearing model performance on various sized rotors with and without centrifugal and gyroscopic forces. Mechanism and Machine Theory, 2015. Vol. 90. pp. 240-260.

[6] Sopanen, J. & Mikkola, A. Dynamic model of a deep-groove ball bearing including localized and distributed defects. Part 1: Theory. Proceedings of the Institution of Mechanical Engineers Part K Journal of Multi-body Dynamics, 2003. Vol. 217. pp. 201-211.

[7] Sopanen, J. & Mikkola, A. Dynamic model of a deep-groove ball bearing including localized and distributed defects. Part 2: Implementation and results. Proceedings of the Institution of Mechanical Engineers Part K Journal of Multi-body Dynamics, 2003. Vol. 217. pp. 213-223.

[8] Ecker, H. Nonlinear stability analysis of a single mass rotor contacting a rigid backup Bearing. Proceedings of the Euromech Colloquium, Loughborough, UK, 1998. pp. 79–89.

[9] Sun, G. Rotor drop and following thermal growth simulations using detailed auxiliary bearing and damper models. Journal of Sound and Vibration, 2006. Vol. 289:1-2. pp. 334-359.

[10] Zeng, S. Modeling and experimental study of the transient response of an active magnetic bearing rotor during rotor drop on back-up bearings. Proceedings of the Institution of Mechanical Engineers, Part I: Journal of Systems and Control Engineering, 2003, Vol. 217: 6. pp. 505-517.

[11] Kirk, R. G. & Ishii, T. Transient response drop analysis of rotors following magnetic bearing power outage. Proceedings of MAG '93: Magnetic Bearings, Magnetic Drives, and Dry Gas Seals Conference and Exhibition, Alexandria, Virginia, 1993. pp. 53-61.

[12] Ishii T, Kirk RG. Transient Response Technique Applied to Active Magnetic Bearing Machinery During Rotor Drop. ASME Journal of Vibration and Acoustics, 1996. Vol. 118:2. pp. 154-163.

[13] Jin, C., Zhu, Y., Xu, L., Xu, Y. & Zheng, Y. The thermodynamic properties of a new type catcher bearing used in active magnetic bearings system. Applied Thermal Engineering, 2015. Vol. 82. pp. 253-263.

[14] Pandiyarajan, R. Starvin, M. S. & Ganesh, K. C. Contact stress distribution of large diameter ball bearing using Hertzian Elliptical contact theory. Procedia Engineering, 2012. Vol. 38. pp. 264-269.

[15] Sun, G. Auxiliary bearing life prediction using Hertzian contact bearing model. Journal of Vibration and Acoustics, 2006. Vol. 128:2. pp. 203-209.

[16] Onal, O., Canadinc, D., Sehitoglu, H., Verzal, K. & Jiang, Y. Investigation of rolling contact crack initiation in bainitic and pearlitic rail steels. Fatigue and Fracture of Engineering Materials and Structures, 2012. Vol. 35:11. pp. 985-997.

[17] Ekberg, A., Kabo, E. & Andersson, H. An engineering model for prediction of rolling contact fatigue of railway wheels. Fatigue and Fracture of Engineering Materials and Structures, 2002. Vol. 25:10. pp. 899-909.

[18] Lee, J.G. & Palazzolo A. Catcher bearing life prediction using a rainflow counting approach. Journal of Tribology, 2012. Vol. 134:3. pp. 031101. 1-14.

[19] Helfert, M. Analysis of anti-friction bearings by means of high-speed videography. Experimental analysis of the retainer bearing behavior after touchdown of a magnetically suspended rotor. Tribologie und Schmierungstechnik, 2008. Vol. 55:1. pp. 10-15.

[20] Khonsari, M. M. & Booser, E. R. Applied Tribology: Bearing Design and Lubrication. Second Edition. John Wiley & Sons. England, 2008. 578 p.

[21] Sopanen, J., Heikkinen, J. & Mikkola, A. Experimental verification of a dynamic model of a tube roll in terms of subcritical superharmonic vibrations. Mechanism and Machine Theory, 2013. Vol. 64. pp. 53-66.

[22] Kärkkäinen, A. Dynamic Simulations of Rotors during Drop on Retainer Bearings. Doctoral Thesis. Lappeenranta University of Technology, Department of Mechanical Engineering, 2007. 91 p. [Referred 24.12.2016]. Available in PDF-File: http://www.doria.fi/bitstream/handle/10024/31108/TMP.objres.728.pdf?sequence=1

[23] Harris, T. A. & Kotzalas, M. N. Rolling Bearing Analysis: Essential Concepts of Bearing Technology. Fifth Edition. Taylor & Francis Group. New York, 2006. 392 p.

[24] Greenwood, J. A. Analysis of elliptical Hertzian contacts. Tribology International, 1997. Vol. 30:3. pp. 235-237.

[25] Brewe, D. E. & Hamrock, B. J. Simplified solution for elliptical-contact deformation between two elastic solids. Journal of Lubrication Technology 1977. Vol. 99:4. pp. 485-487.

[26] Hamrock, B. J. & Brewe, D. E. Simplified solution for stresses and deformations. Journal of Lubrication Technology, 1983. Vol. 105:2. pp. 171-177.

[27] Korolev, A. V., Korolev, A. A. & Krehel, R. Character of distribution of the load between the balls in the ball bearings under the action combined of external load. Mechanism and Machine Theory, 2014. Vol. 81. pp. 54-61.

[28] Oswald, F. B., Zaretsky, E. V. & Poplawski, J. V. Effect of Internal Clearance on Load Distribution and Life of Radially Loaded Ball and Roller Bearings. Technical Report. NASA, Prepared for the 65th Annual Meeting and Exhibition sponsored by the Society of Tribologists and Lubrication Engineers, 2012. NASA/TM-2012-217115. 39 p. [Referred 1.1.2016]. Available: http://ntrs.nasa.gov/archive/nasa/casi.ntrs.nasa.gov/20120008398.pdf

[29] Göncz, P., Ulbin, M. & Glodež, S. Computational assessment of the allowable static contact loading of a roller-slewing bearing′s case-hardened raceway. International Journal of Mechanical Sciences, 2015, Vol. 94-95. pp. 174-184.

[30] Wang, Y. & Yuan, Q. Contact Force Distribution and Static Load-carrying Capacity of Large Size Double Row Four-point Contact Ball Bearing. Defence Technology, 2013. Vol. 9:4. pp. 229-236.